Chemical Science

ROYAL SOCIETY OF CHEMISTRY

REVIEW

View Article Online
View Journal | View Issue

Cite this: *Chem. Sci.*, 2025, **16**, 4937

Biomass-derived carbon dots: synthesis, modification and application in batteries

Dongyang Cai,[a] Xue Zhong,[a] Laiqiang Xu, *[b] Yu Xiong, *[a] Wentao Deng,[a] Guoqiang Zou,[a] Hongshuai Hou *[a] and Xiaobo Ji [a]

Biomass-derived carbon dots (BCDs) have attracted considerable attention for their promising attributes, including low toxicity, excellent solubility, biocompatibility, and eco-friendliness. Their rich surface chemistry and impressive photoluminescent properties have sparked widespread research interest, particularly in areas such as sensing and biomedicine. However, the potential applications of BCDs in the energy sector, especially in electrochemical energy storage batteries, have received scant review focus. This article systematically consolidates the selection of carbon sources, synthesis methods, modification strategies, and the corresponding characterization techniques for BCDs. Application strategies in energy storage batteries are explored, with the underlying connection between the role of BCDs in batteries and their structural properties being analyzed, providing comprehensive insights from synthesis and characterization to application. Furthermore, a preliminary discussion is initiated on the current limitations in material regulation and design within research, and potential avenues for enhancement are proposed.

Received 23rd December 2024
Accepted 23rd February 2025

DOI: 10.1039/d4sc08659g

rsc.li/chemical-science

1. Introduction

Carbon dots (CDs) are a new type of zero-dimensional materials with a size of 2–10 nm.[1] Since they were discovered by Xu *et al.*,[2] they have received an increasing amount of attention due to their significant advantages in terms of low toxicity, favorable biocompatibility, chemical stability, outstanding water solubility, abundant surface functionalities, facile modification, and unique optical properties.[3,4] They typically consist of a carbon-based core with sp^2/sp^3 domains and various chemical functional groups on the surface (Fig. 1a–c). Based on different core structures, photoluminescence behaviors, and carbon precursors,[6] they can be classified into four types (Fig. 1b): graphene quantum dots (GQDs),carbonized polymer dots (CPDs), carbon nanodots (CNDs), and carbon quantum dots (CQDs). However, due to the need for further study on the structure and formation mechanism of carbon dots, strict classification is challenging,[9] and there are many differing views within the academic community. Valcárcel *et al.*[10] proposed that small fragments of a single atomic layer of graphite (<20 nm) be

[a]*College of Chemistry and Chemical Engineering, Central South University, Changsha, 410083, China. E-mail: hs-hou@csu.edu.cn; thomas153@126.com*

[b]*Key Laboratory of Renewable Energy Electric-Technology of Hunan Province, School of Energy and Power Engineering, Changsha University of Science and Technology, Changsha, 410114, China. E-mail: lq-xu@csust.edu.cn*

Dongyang Cai

Dongyang Cai is currently pursuing his Master's degree at the School of Chemistry and Chemical Engineering, Central South University (CSU) under the supervision of Prof. Xiaobo Ji and Prof. Hongshuai Hou, and received his BSc degree from CSU in 2024, with his current research focusing on the design and synthesis of cathode materials for Na–S batteries.

Laiqiang Xu

Dr Xu is a lecturer at the School of Energy and Power Engineering, Changsha University of Science and Technology. He received his PhD in Physical Chemistry of Metallurgy from Central South University under the supervision of Prof. Xiaobo Ji. His research interests focus on electrochemistry and key materials for electrochemical energy storage devices.

termed GQDs, while spherical carbon dots exhibiting quantum confinement and crystalline structures are denoted as CQDs. Additionally, amorphous quasi-spherical nanoparticles lacking quantum confinement are classified as CNDs. Wareing *et al.*[11] categorized carbon dots into two types (graphene quantum dots (GQDs) and amorphous CDs), and pointed out that the distinction between the two types of quantum dots remains unclear, but both should be classified as part of the CD (carbon dot) family. For the sake of precision and accuracy, in this review, we adopt the term "carbon dots (CDs)" to collectively refer to zero-dimensional fluorescent carbon nanomaterials, without delineating their definitions. However, it's noteworthy that discrepancies in factors such as carbon source selection and synthesis methods can yield varying CD structures, subsequently impacting their properties, including photoluminescent characteristics and surface chemistry, among others.

Several effective methods for synthesizing carbon dots are available, including both top-down and bottom-up approaches (Fig. 1d). Top-down methods involve breaking down large carbon sources such as graphite,[12] graphene,[13] CNTs,[14] and fullerene[15] into nanoparticles through techniques such as laser ablation,[16] electrochemical methods,[17] ball-milling,[9] arc discharge,[18] and chemical oxidation.[19] The bottom-up approach refers to synthesizing carbon dots through a "polymerization–carbonization" process,[3] wherein small molecule precursors are transformed using methods such as hydrothermal carbonization (HTC), solvothermal, microwave hydrothermal, pyrolysis carbonization, and more. However, the majority of carbon dot synthesis relies on carbon sources derived from expensive, unsustainable, or even toxic chemical reagents.[20] These include graphene, carbon nanotubes, petroleum by-products, polycyclic aromatic hydrocarbons,[21,22] aniline, polyphenols,[23] and more. Furthermore, their processing often involves the use of strong acids or bases and demanding conditions with high energy consumption.[24] These factors impede the widespread adoption and production of carbon dot materials, prompting the search for low-cost, sustainable, and environmentally friendly carbon sources and processes. Biomass, with its widespread availability, low cost, high carbon content, green safety profile, and ease of conversion into carbon dots, emerges as an ideal carbon source. Carbon dots derived from biomass typically exhibit outstanding fluorescence properties and biocompatibility.[25,26] Consequently, current research predominantly concentrates on their applications in sensors, optical materials, biomedical imaging, and pharmaceuticals (Table 1). In fact, BCDs have demonstrated significant potential in the fields of energy storage and conversion, owing to their tunable carbon cores and abundant surface functional groups.[36,37] These carbon dots, particularly in fields such as electrocatalysis, rechargeable batteries, and fuel cells, not only offer a green and cost-effective approach to material design, but also play a crucial role in the construction of active sites and the regulation of surface and interface properties.[38] This review aims to explore recent advancements in the synthesis and application strategies of BCDs, with a specific focus on their applications in rechargeable batteries, thereby providing new insights and directions for future research and development in this field (Fig. 2).

2. Synthesis

2.1 Biomass carbon sources

The distribution and range of biomass carbon sources are incredibly vast, encompassing all living organisms-plants, animals, and microorganisms-that produce renewable products through biological metabolic processes like photosynthesis and respiration.[35,39] From the perspective of raw materials, they can be categorized into two groups: complex organisms such as ginkgo leaves,[40] grass,[41] grapefruit peel,[42] branches,[43] wood shavings,[44] lemon juice,[45] milk,[46] eggshell membranes,[47] wool,[48] and cow dung,[49] among others, and relatively simple biomass components, including macromolecules and small molecules[50] like glucose,[51] citric acid,[52] natural amino acids,[53] starch,[54] cellulose,[28] chitin,[55] and natural proteins.[56] It's noteworthy that utilizing organisms directly as raw materials is typically cost-effective, with preprocessing procedures remaining relatively simple, often involving basic cleaning, drying, or shredding (Fig. 3). During processing, the sugars, vitamins, and pectin abundant in plants, or the proteins and trace elements found in animal derivatives, can undergo polymerization and carbonization at high temperatures (Fig. 3b and c), forming a carbon

Yu Xiong

Yu Xiong received his PhD degree from Central South University, and he has spent two years at Tsinghua University as a Postdoctoral Researcher under the supervision of Prof. Yadong Li. He is currently working as an Associate Professor at Central South University. His research interests focus on the synthesis and the electrocatalytic performance of single-atom catalysts.

Hongshuai Hou

Dr Hou is a Professor at the College of Chemistry and Chemical Engineering, Central South University. He received his PhD from Central South University in 2016. His current research interests are new carbon dot-based materials and electrochemical energy storage materials.

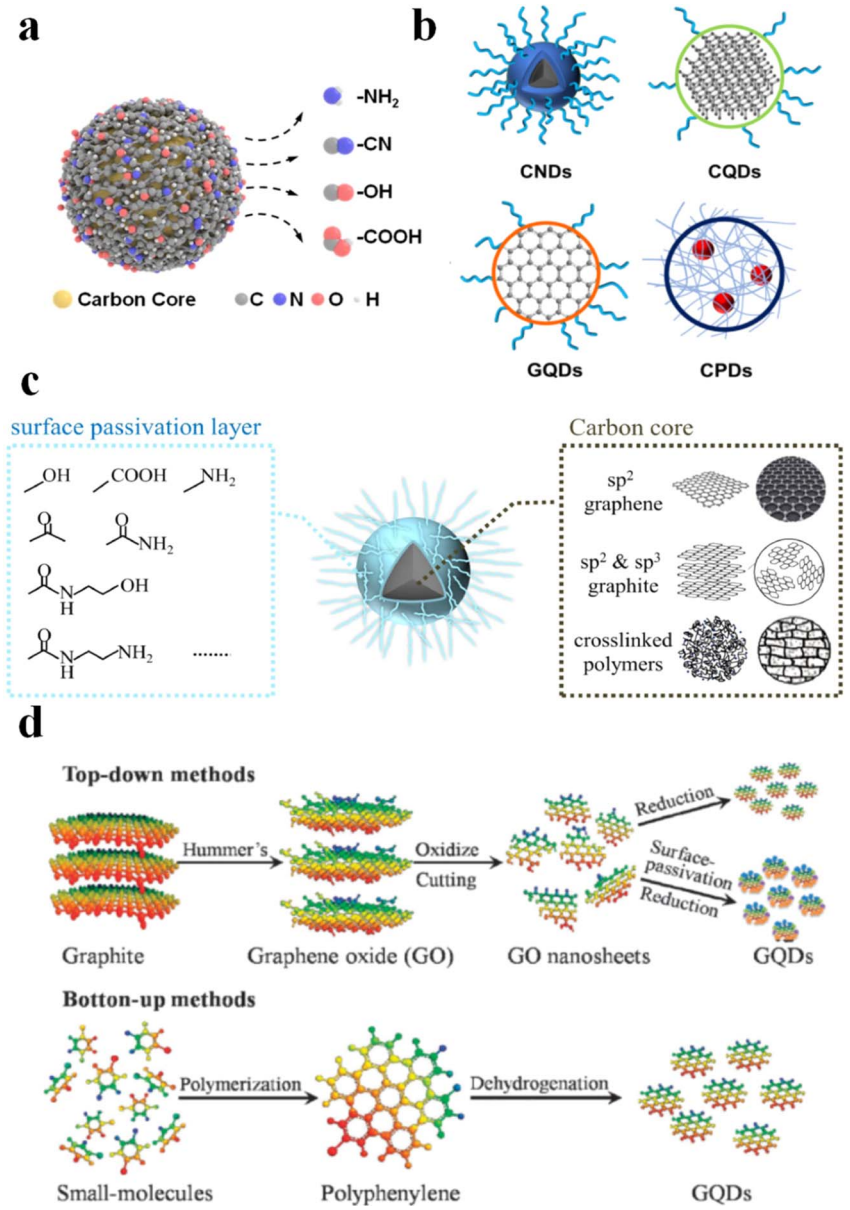

Fig. 1 Overview of the structure and synthesis of carbon dots: (a) schematic illustration of a kind of CD. Reproduced with permission.[5] Copyright 2023, American Chemical Society; (b) classification of the four carbon dots based on different core structures. Reproduced with permission.[6] Copyright 2024, Elsevier; (c) schematic of the structures of CDs. Reproduced with permission.[7] Copyright 2021, Elsevier; (d) schematic diagram of the top-down and bottom-up methods for synthesizing GQDs. Reproduced with permission.[8] Copyright 2012, Royal Society of Chemistry.

skeleton that leads to the creation of fluorescent CDs.[3] Additionally, heteroatoms such as nitrogen, phosphorus, and sulfur inherent in the organisms themselves can be naturally doped into CDs, imparting various abundant functional groups onto the CD surfaces, thereby enhancing their fluorescence efficiency and surface properties. However, the composition of natural organisms is intricate, and variations between organisms can introduce instability into product structure regulation. For instance, Karahan *et al.*[60] proposed in their experiment utilizing watermelon seeds for the preparation of carbon dots that understanding the composition of biomass substrates is essential for gaining deeper insights into the formation mechanism of carbon dots. Watermelon seeds, comprising 30% lignin, 39.17% cellulose, and around 20% hemicellulose, yielded two distinctly different carbon materials in this study, which were respectively applied in lithium-ion batteries and cellular imaging fields. This underscores the intricate nature of organisms' carbon sources and the variability in their resultant products. Another example stems from the research conducted by Reisner *et al.*,[61] which vividly depicts the compositional disparities among various parts of the same organism (α-cellulose, xylan, and lignin) (Fig. 3a). Using pure reagents derived from different biological derivatives (α-cellulose, citric acid (CA), and aspartic acid) for identical heat treatments

Table 1 The main content of the recent reviews on BCDs

Title	Time	Emphasis	Application	Ref.
Biomass-based carbon dots: current development and future perspectives	2021	Comparison of semiconductor quantum dots, chemical carbon dots, and biomass derived carbon dots. Synthesis process of biomass derived carbon dots, and biomedical applications	Sensors, bioimaging, drug carriers, and electrical applications	11
Biomass-derived carbon dots and their applications	2019	Selection of the biomass carbon source, hydrothermal synthesis, optical properties of BCDs, and applications in sensing and biomedical imaging	Sensing, drug delivery, bioimaging, solar cells, and catalysis	27
Lignocellulosic biomass-based carbon dots: synthesis processes, properties, and applications	2023	The process of using wood cellulose as a carbon source, the formation mechanism, structural characteristics, optical features, materials related to optical characteristics, and manufacturing of intelligent responsive materials	Sensors, information encryption, optical functional films, catalysis, optronics, photothermal conversion, supercapacitors, and bioimaging	28
Functional carbon dots derived from biomass and plastic wastes	2023	CDs derived from biomass and plastic waste, their preparation, structure, properties, and applications. The application of materials compounded with polymers	Optical applications, supercapacitors, chemical detection application, and biological applications	29
State-of-the-art of biomass-derived carbon dots: preparation, properties, and applications	2024	The optical properties, low-cost preparation, and application advantages of biomass-derived carbon dots	Optical imaging, sensors, and phototherapy	30
Carbon dots: synthesis, formation mechanism, fluorescence origin and sensing applications	2019	Green synthesis of carbon dots (including selection of biomass carbon sources and other carbon sources, and sustainable processes), exploration of the fluorescence mechanism of carbon dots, and their applications in sensing	Solution phase sensing and solid phase sensing	3
A review on the synthesis, properties, and applications of biomass derived carbon dots	2023	Selection of green carbon sources, characterization methods and the properties of carbon dots, effects of doping, and applications in sensing and fluorescence	Fluorescence and electrochemical sensing, fluorescent ink, photocatalytic applications, and pharmaceutical applications	31
Biomass-waste derived graphene quantum dots and their applications	2018	The chosen carbon source is biomass waste, exploring some influencing factors in synthesis, sensing, luminescence, biomedical applications of BCDs, and energy applications of graphene quantum dots	Applications of biomass derived GQDs: PL sensors, light-emitting diodes, and biomedical applications Energy applications of GQDs in general: supercapacitors, batteries, and photovoltaics	24
Carbon quantum dots derived from polysaccharides: chemistry and potential applications	2024	Various polysaccharides as carbon sources, and applications in the environment, textile industry, and medical fields	Soil fertilization, detection of heavy metals, textile finishing, and biological activities (microbicidal, anticancer & antiviral activities)	32
Construction of biomass carbon dot based fluorescence sensors and their applications in chemical and biological analysis	2019	Applications of biomass carbon dots in the sensing field, including the preparation of sensors and quenching mechanisms of biomass CDs	Metal ion sensors, anion sensors, small molecule sensors, macromolecule sensors, and bioimaging	33
Synthesis and applications of carbon quantum dots derived from biomass waste: a review	2023	The factors influencing the performance of biomass carbon dots, their optical properties, and applications in energy, the environment, and medicine-related fields	Energy storage batteries, energy storage supercapacitors, renewable energy, pollutant sensing, catalytic degradation of environmental pollutants, drug delivery, biosensing, and bioimaging	34
Recent advances of biomass carbon dots on syntheses, characterization, luminescence mechanism, and sensing applications	2021	Using animals, plants and their derivatives, as well as urban waste as carbon sources; methods to control the optical properties of carbon dots and tune fluorescence color and quantum yield; summarizing the luminescence mechanism and quenching mechanisms in detection applications	Sensing	35

Fig. 2 Overview of BCDs: from biomass carbon sources to battery applications.

resulted in carbon dots with markedly different properties. Thus, relying solely on organisms as carbon sources may pose challenges in achieving the desired carbon dot products. There might be opportunities for further exploration in understanding biomass components and optimizing purification processes. Furthermore, the relatively low content of active substances capable of participating in reactions within natural organisms may limit the efficiency of carbon dot production. Although the abundance of raw materials can offset this limitation, it remains a crucial consideration in the carbon source selection process. Opting for relatively pure biological components like glucose, citric acid (CA), or cellulose as raw materials can mitigate some stability concerns but may elevate production costs.

2.2 Synthesis methods of carbon dots from biomass carbon sources

The synthesis methods of BCDs include various techniques such as HTC, solvothermal methods, microwaves, chemical oxidation, and pyrolysis carbonization.

2.2.1 Microwave-assisted synthesis. Microwave carbonization stands out as a remarkably convenient, cost-effective, and highly efficient method for carbon dot synthesis.[62] By harnessing the energy of electromagnetic waves, it disrupts chemical bonds within biomass materials, prompting dehydration, polymerization, and ultimately carbonization to yield carbon nanostructures.[34] Despite its minimal time requirements and comparatively high carbon dot and quantum yields,[11] drawbacks include limited control over reaction conditions and product sizes, along with potential health risks associated with microwave radiation.[29,33] Nevertheless, studies have successfully employed microwave techniques to synthesize carbon dots from diverse sources like garlic,[63] flour,[64] and roses.[65]

2.2.2 Chemical oxidation approach. The chemical oxidation approach involves the use of potent oxidizing agents such as hydrogen peroxide and nitric acid[66] to catalyze the carbonization of biomass materials. This method introduces hydrophilic surface functional groups, like hydroxyl and carboxyl groups, rendering it a simple, effective, and scalable technique.[11] However, the use of costly and hazardous oxidants raises concerns about material toxicity, somewhat conflicting with the environmentally friendly ethos of biomass utilization, leaving room for optimization.

2.2.3 Pyrolysis carbonization. Pyrolysis carbonization is a commonly employed method, where a carbon source is placed in an inert gas atmosphere, at controlled pressure and elevated temperatures (>350 °C). The precursor undergoes a sequence of dehydration, polymerization, and carbonization, ultimately yielding carbon dots.[29] The pyrolysis method offers relatively straightforward steps and swift processing. Moreover, unlike the microwave method, it isn't constrained by the requirement of using water as a solvent.[27] Nonetheless, its high-energy

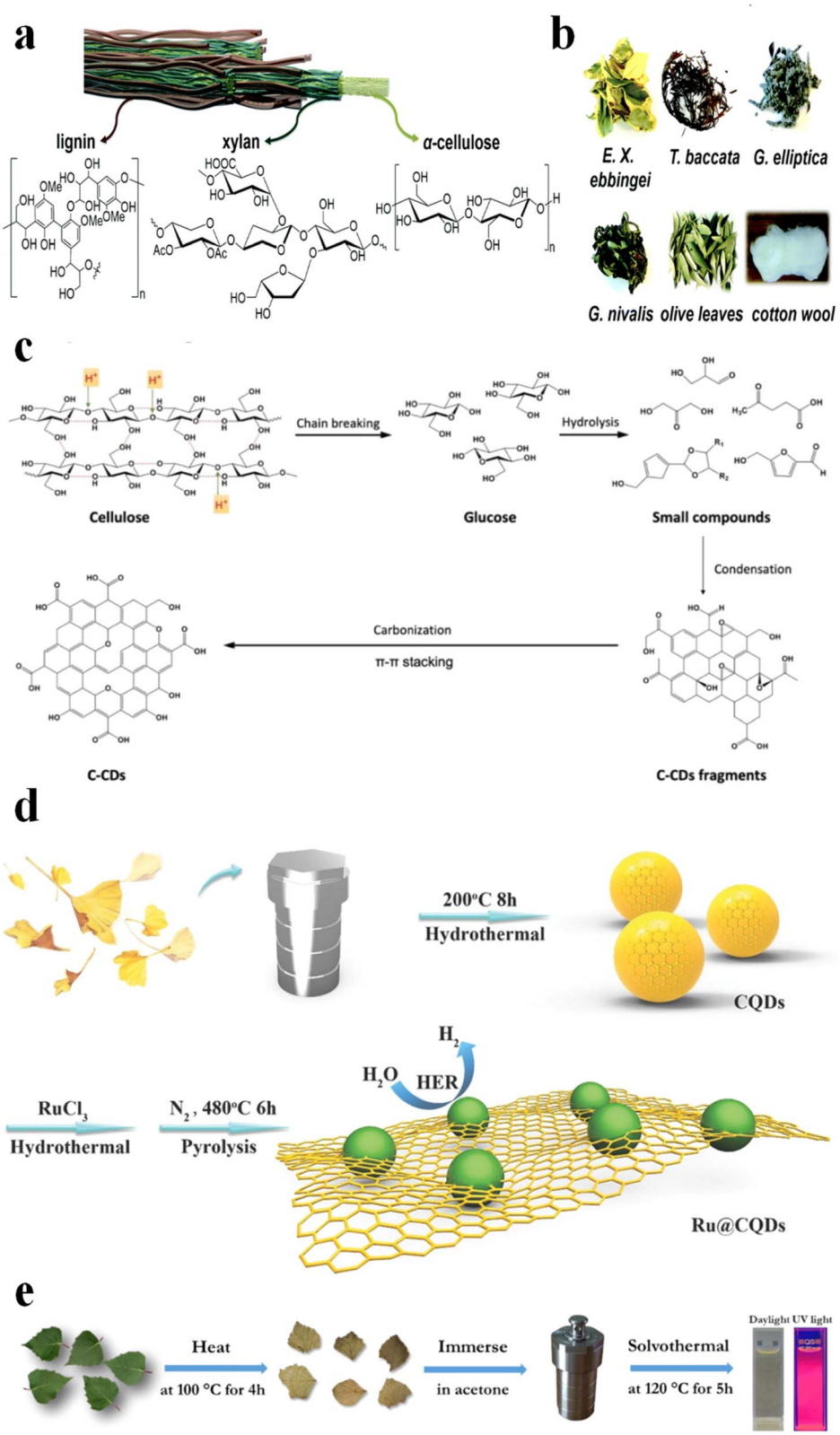

Fig. 3 Carbon source selection for synthetic BCDs: (a) schematic representation of the lignocellulosic structure and the complex chemical composition of the carbon source of the same organism; (b) optical images of biomass waste used for the synthesis of CDs. Reproduced with permission.[57] Copyright 2020, Royal Society of Chemistry; (c) cellulose chain breaking, hydrolysis, polymerization, and carbonization. Reproduced with permission.[28] Copyright 2023, Wiley-VCH; (d) carbon dots were synthesized from leaves of *Ginkgo biloba* as a carbon source for electrocatalysis. Reproduced with permission.[58] Copyright 2018, Wiley-VCH; (e) the process of synthesizing carbon points with birch leaves, for sustainable electroluminescent devices. Reproduced with permission.[59] Copyright 2023, Royal Society of Chemistry.

consumption and the wide particle size distribution of resultant products signify areas for improvement.[29]

2.2.4 Hydrothermal carbonization. Hydrothermal carbonization (HTC) stands out as the foremost method for producing BCDs, primarily because various biomolecules exhibit remarkable water solubility or hydrophilicity (Fig. 3d and e). This characteristic facilitates the efficient dispersion of a diverse array of molecules and ions within the reaction milieu. Within the confines of a sealed pressure vessel, under conditions of elevated temperature and pressure, biomass feedstocks undergo a sequence of transformations including condensation (comprising hydrolysis, dehydration, and decarboxylation processes), polymerization, aromatization, and passivation.[60] These intricate processes culminate in carbonization, giving rise to the formation of carbon dots. For example, experiments conducted by Baccile *et al.*[67] unveiled the generation of dehydration intermediates such as hydroxymethylfurfural and furfural during the hydrothermal treatment of various biomasses (including glucose, xylose, maltose, sucrose, amylopectin, and starch). Subsequently, these intermediates proceed to undergo further condensation, resulting in the formation of other carbon structures. Karak *et al.*[68] synthesized water-soluble fluorescent carbon dots from banana juice, utilizing carbohydrates like fructose, sucrose, glucose, and ascorbic acid as carbon sources. The mechanism they suggest for formation begins with the hydrolysis, dehydration, and subsequent decomposition of carbohydrates when ascorbic acid is present. This process results in the creation of various soluble compounds, including furfural, different types of aldehydes, ketones, and several organic acids such as acetic, levulinic, and formic acid. These compounds undergo polymerization and condensation to form various soluble polymer products. Following this, aromatic restructuring and carbonization occur through condensation and cyclization reactions. Ultimately, carbon dots are formed through a likely nucleation burst of aromatic clusters at a critical concentration at the supersaturation point.

During the hydrothermal carbonization process, many materials retain their inherent functional groups containing oxygen, such as carboxyl and hydroxyl groups.[69] This offers the opportunity to introduce additional materials post-hydrothermal reaction or through functionalization, thereby further enhancing the physicochemical properties of HTC materials.[39] Additionally, the heteroatoms naturally present in the biomass feedstock undergo self-doping during this process. For example, Feng *et al.*[70] utilized winter melon juice as both the biomass carbon source and the self-doping nitrogen source to synthesize photoluminescent N-doped carbon dots, demonstrating their excellent biocompatibility and promising applications as bio-imaging agents.

In summary, hydrothermal carbonization represents a synthesis approach characterized by simplicity in operation, environmental friendliness, cost-effectiveness, ease of control, and scalability. Nonetheless, the precise effects of various reaction parameters-such as temperature, duration, concentration, and others-on the structure (encompassing size, carbonization extent, surface functional groups, *etc.*) and yield of carbon dot products remain ambiguous. Hence, there arises a need for deeper exploration into the mechanisms and processes governing hydrothermal reactions, aiming for enhanced predictability, construction of product structures, and refinement of production conditions.

For instance, Huang *et al.*[71] observed that employing ginkgo wood for the synthesis of wood-based carbon quantum dots, under optimal conditions of 180 °C for 8 hours resulted in maximal photoluminescence intensity of the carbon dot products. They emphasized that deviations from these conditions-either inadequate carbonization due to insufficient time or low temperature, or excessive carbonization due to prolonged time or elevated temperature-resulted in diminished photoluminescence intensity of the wood-based carbon quantum dots.

In another study, Sapelkin *et al.*[72] investigated the hydrothermal reaction of glucose for carbon dot production. They noted that extending the reaction time led to reductions in carbon dot particle size and enhancements in monodispersity. In-depth investigations using high-resolution transmission electron microscopy (HRTEM) and diffraction analysis indicated a decrease in crystallinity and phases. Meanwhile, Raman spectroscopy results pointed to an enhancement in crystallinity, evidenced by a decreased I_D/I_G ratio and narrower G-band width. The research suggested a plausible structure for carbon dots, consisting of a graphitic sp^2 carbon core that is functionalized with peripheral carboxylic and carbonyl groups, as well as sp^3 carbon defects. Additionally, a mechanism for the formation of carbon dot particles was outlined, encompassing four distinct stages: precursor decomposition, polymerization and aromatization, nucleation, and subsequent growth. The solvothermal method serves as an extension of the hydrothermal approach, utilizing organic solvents like ethanol, acetone, DMF, *etc.*, as substitutes for water, or employing mixed solvents such as ethanol–water solutions. For instance, Packirisamy *et al.*[73] conducted solvothermal treatment using a 25 vol% ethanol–water solution with a non-aqueous carbon source, curcumin. This yielded highly hydrophilic BCDs, and they further explored their potential application in bioimaging.

3. Modification strategies of biomass-derived carbon dots

The synthesis of BCDs involves various modification methods, with common approaches including heteroatom doping and surface functionalization. The introduction of heteroatoms into carbon dots affects the Fermi level and electrons in the conduction band, thereby altering their optical and surface properties. Doping methods mainly comprise self-doping within biological entities and the addition of exogenous doping reagents such as urea, ethylenediamine (EDA), and sodium thiosulfate.[74]

Lu *et al.*[75] conducted a study where they prepared three types of carbon dots using CA as the carbon source (Fig. 4): nitrogen-free CA-CDs, nitrogen-doped CE-CDs with EDA, and nitrogen-doped CM-CDs with melamine. They characterized CM-CDs

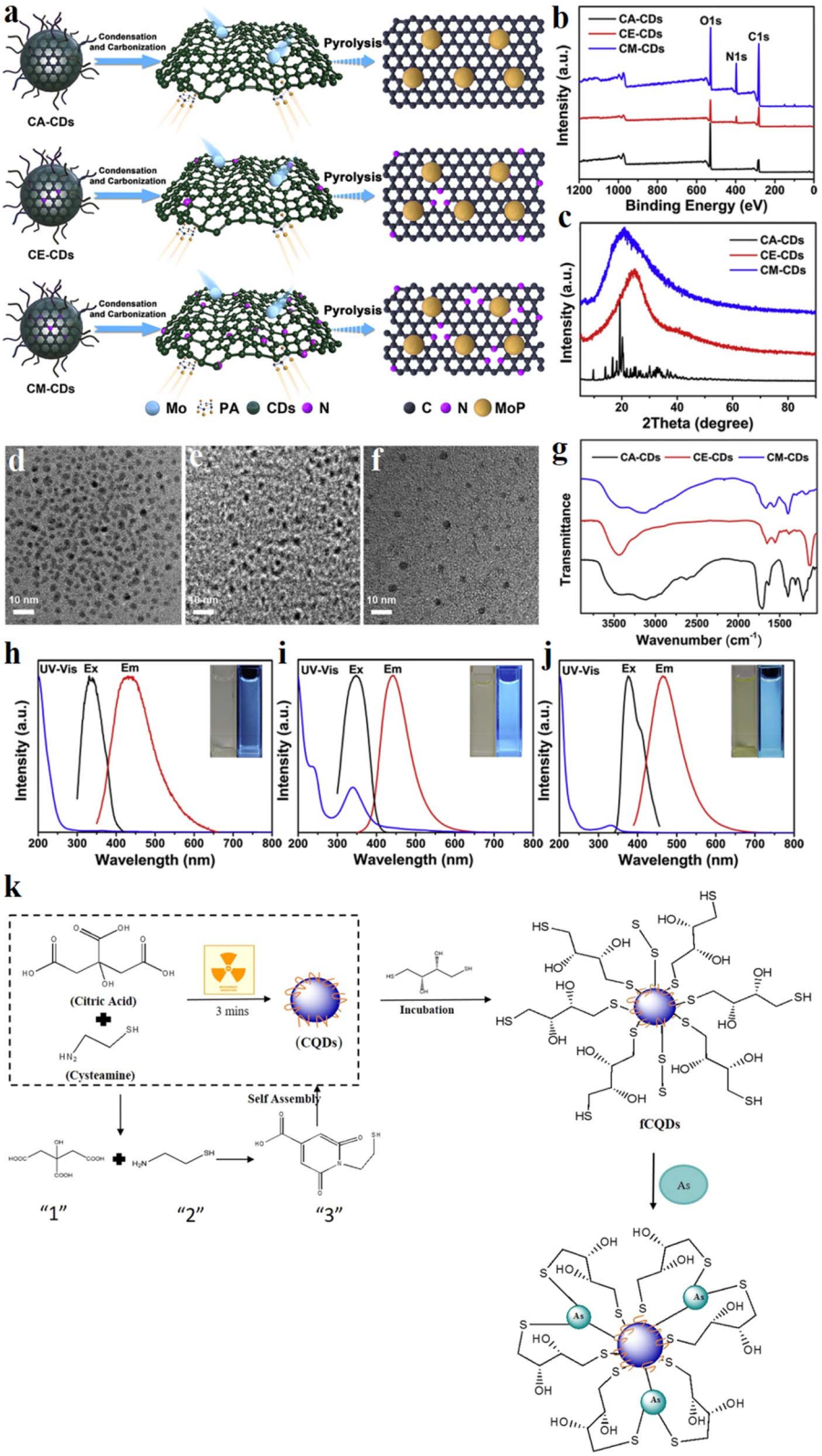

Fig. 4 Modification methods of BCDs: (a) a schematic representation of the synthetic pathway used to prepare the N-doped and defect-engineered MoP/CDs catalyst; (b) XPS survey spectra of CDs; (c) XRD patterns; (d)TEM images of CA-CDs, (e) CE-CDs and (f) CM-CDs; (g) FT-IR spectra; (h) PL excitation, UV-vis absorption and PL emission spectra of the CA-CDs, (i) CE-CDs, and (j) CM-CDs, and insets display images of the CDs in aqueous solution, with the left side showing their appearance under visible light and the right side under UV light. (a–j) Reproduced with permission.[75] Copyright 2020, Elsevier; (k) schematic of synthesis and functionalization of CDs and the proposed binding approach with arsenite. Reproduced with permission.[76] Copyright 2017, Elsevier.

with the highest nitrogen content through X-ray photoelectron spectroscopy (XPS) (Fig. 4b). Transmission electron microscopy (TEM) images revealed different particle sizes among the three materials (Fig. 4d–f). X-ray powder diffraction (XRD) indicated the broad (002) plane peaks for CE-CDs and CM-CDs, corresponding to an amorphous carbon structure, suggesting that they are amorphous carbon materials (Fig. 4c). UV-vis absorption spectra, and PL excitation and emission spectra of the three materials also exhibited noticeable differences (Fig. 4h–j). Fourier-transform infrared spectroscopy (FT-IR) characterization showed that nitrogen doping led to different N-containing functional groups on the surface of carbon dots (Fig. 4g). In subsequent studies, carbon dots were mixed with Mo compounds and phytic acid (PA) as raw materials, followed by pyrolysis in an argon atmosphere to form catalysts for water electrolysis. The research highlighted that during pyrolysis, carbon dots underwent self-crosslinking *via* hydrogen bonds between surface functional groups (*e.g.*, amino ($-NH_2$), hydroxyl (–OH), and carboxyl (–COOH) groups) and van der Waals bonding between adjacent carbon dots, forming interconnected carbon layers. These carbon layers exhibited good electrical conductivity and helped reduce the internal resistance of materials. Furthermore, the study emphasized that by selecting appropriate precursor molecules for the synthesis of carbon dots, the doping of carbon dots with different heteroatoms could be controlled, thereby adjusting the electron arrangement of surrounding reaction sites. The doping of nitrogen introduced defects and increased the number of active sites on the surface of carbon dots. Nitrogen-doped carbon dots enhanced catalytic activity, reduced the overpotential of the catalyst, and strengthened the adsorption capacity of reaction intermediates, thereby significantly improving the catalytic performance of the catalyst.

Self-doped carbon dots can be prepared by employing the biomass precursors containing heteroatoms. For example, Ding *et al.*[77] utilized the sulfur-rich tropical fruit durian as a carbon source to synthesize sulfur-doped carbon dots. The luminescent properties of these CDs can be finely adjusted by controlling the degree of S doping and demonstrate high quantum yields, highlighting their potential applications in fluorescence bioimaging. In another study, Ge *et al.*[78] employed green pepper seeds as a carbon source to hydrothermally synthesize nitrogen, sulfur, and phosphorus co-doped carbon dots (NSP-CDs). These NSP-CDs exhibit remarkable fluorescence properties, water solubility, and biocompatibility, showcasing their promising role as biological fluorescent probes.

Surface functionalization or surface passivation refers to improving the performance of carbon dots (CDs) by modifying functional groups on their surface without altering the carbon core, thereby influencing their properties, including surface chemistry and optical performance. For example, Pooja D. and her team[76] synthesized nitrogen/sulfur-doped carbon dots through self-assembly by dehydrating and condensing bio-derived precursors such as CA and cysteamine using a simple microwave pyrolysis method (Fig. 4k). It was noted during the synthesis of the intermediate (Fig. 4k "3") that CA and cysteamine experienced the removal of three water molecules, resulting in surface passivation, which introduced nitrogen and sulfur groups to varying degrees. The presence of thiol functional groups on the surface of CDs was confirmed by FT-IR. Functionalization of carbon dots with dithiothreitol was performed to impart thiol functional groups on their surface for selective detection of toxic arsenite in water. The study also explored the absorption and emission properties of CDs following functionalization. It was found that the positioning of the peaks remained unchanged when thiol ligands were introduced. Furthermore, the emission behavior of the CDs post-functionalization, across various excitation wavelengths, demonstrated excitation-independent characteristics. This suggests that dithiothreitol primarily added surface functionalities to the CDs without altering their internal architecture.

Research on the doping and surface functionalization of BCDs is still in its nascent stages, with much inspiration drawn from the self-doping processes of biomass materials.[79] In reality, the synthesis of BCDs isn't inherently incompatible with that of chemical carbon dots; rather, they share numerous similarities and offer opportunities for mutual enhancement. While some dopants like EDA, thiourea, and melamine may not originate from biological sources, they have been proven to significantly enhance material functionality when used as exogenous dopants in biomass carbon dot synthesis, even in small quantities. It's important to note that this doesn't fundamentally contradict the principles of green synthesis. Furthermore, biologically derived dopants such as urea, amino acids, and phytic acid present alternative, eco-friendly doping avenues. This realm of research remains ripe for further exploration. Moreover, given the typically abundant presence of functional groups on biomass carbon dot surfaces, there exists immense potential for surface functionalization. As investigations into various biomass carbon dot structures deepen, adopting modification strategies for chemical carbon dots could prove to be a fruitful avenue for future inquiry.

4. The structural characteristics and corresponding characterization techniques of BCDs

Due to the extensive applications of BCDs in fields such as fluorescence sensing, bioimaging, and optical materials, there is a wealth of literature discussing their optical properties and control methods. Consequently, we won't delve further into the optical properties of BCDs here. In essence, owing to the "quantum size effect", the fluorescence emission wavelength of BCDs varies with particle size. Carbon dots synthesized through different methods exhibit distinct ultraviolet-visible absorption characteristics, with their excitation wavelength and intensity subject to control by factors such as particle size, pH value, and surface defect status. This endows them with remarkable tunable luminescent properties. Moreover, BCDs may also manifest features such as upconversion fluorescence and downconversion fluorescence.

We will now provide an overview of the structural characteristics and corresponding characterization methods of carbon

dots. This will aid in advancing research on the preparation, modification, understanding of formation mechanisms, and applications of carbon dots.

BCDs typically consist of sp^2-hybridized graphite mixed with a sp^3-hybridized core and surface-hydrophilic oxygen-containing groups. The particle size typically ranges from 2 to 10 nm, and specific structural characterization data are listed in Table 2.

5. Application of BCDs in batteries

5.1 Lithium-based batteries

5.1.1 Lithium-ion batteries. Lithium-ion batteries (LIBs), with the advantages of high output voltage, high energy density, low self-discharge rate, *etc.*, have widespread applications in electronic products, electric vehicles, and other fields.[80–83] However, in these areas, such as the iterative development of electric vehicles, there are increasing demands on the power density and cycle life of LIBs.[84,85] The development of LIBs with high reversible capacity, excellent rate performance, and long-term cycle stability largely depends on the improvement of the slow diffusion kinetics processes and structural stability of the electrodes.[86–89] Among them, the research on optimizing battery materials through various strategies, such as using BCDs, has made some remarkable progress.

Silicon monoxide (SiO) has gained attention as a potential high-capacity anode material for the advancement of rechargeable LIBs in the rapidly expanding realm of portable electronics.[90] However, a significant challenge facing SiO anodes is their poor initial coulombic efficiency (ICE), which is largely attributed to the formation of irreversible Li_ySiO_z compounds and their inherently low conductivity. Consequently, the incorporation of supplementary cathode materials becomes essential to compensate for the lithium ion consumption in full cells, thereby limiting the potential improvement of the actual energy density in LIBs.[91] Moreover, all Si-based anode materials will have a continuous parasitic reaction with the electrolyte. This arises from the substantial, repeated volume changes (~200%) that induce an unstable solid electrolyte interface (SEI) film. Furthermore, the highly reactive lithiated compound Li_xSi may interact spontaneously with the electrolyte. Efforts to mitigate these reactions have focused on the utilization of appropriate electrolyte additives to improve the mechanically and chemically stable solid electrolyte interface films. Additionally, the development of new binders featuring rigid or flexible composite frameworks and self-healing properties has demonstrated efficacy in accommodating large volume expansions and curbing parasitic reactions.[92] Lin *et al.*[44] employed discarded Balsa wood sawdust and lithium bis(trifluoromethane sulfonimide) (LiTFSI) in a single-step hydro/alcohol-thermal reaction to fabricate lithium-absorbed and fluorine-doped CDs possessing heteroatom-rich and lithium-absorbing properties (Fig. 5a–d). The size of the F-CDs-Li nanoparticles is approximately 3 nm. XPS analysis revealed that fluorine in the F-CDs-Li primarily exists as C–F bonds, while lithium mainly adsorbs on the surface of CDs in the form of Li–OH, indicating successful doping of F into CDs and surface adsorption of Li onto CDs (Fig. 5d). Subsequently, silicon monoxide was mixed with a designated volume of F-CDs-Li solution to adsorb F-CDs-Li onto micro-sized SiO particles. The mixture was stirred and dried at 80 °C, followed by heating of the obtained sample at 800 °C in a corundum boat for 5 hours. During the annealing process, the zero-dimensional CDs underwent self-assembly and carbonization, resulting in the formation of a LiF-modified carbonaceous layer that coats the SiO particles. The LiF-carbon coating on the surface of SiO particles facilitates ion/electron transmission, induces the pre-decomposition of $LiPF_6$ to generate a uniform and thin dense SEI with a LiF-rich inner layer, and also suppresses volume expansion of the electrode materials during cycling (Fig. 5e). This inhibition of volume expansion helps in preventing electrolyte reduction and SiO particle fragmentation, thereby significantly enhancing coulombic efficiency (CE), cycle life, and rate performance. Consequently, the SiO@LCD electrode materials demonstrate superior electrochemical properties compared to SiO or LiF-free carbon-coated SiO electrode materials, exhibiting higher average CE and improved cycling stability. The pouch cell assembled at the ampere hour (A h) level exhibits remarkable cycling stability, maintaining a capacity of 3105.4 mA h (capacity retention of 85.1%, 400 cycles at 0.2C) (Fig. 5f).

Two-dimensional (2D) layered materials, renowned for their high specific surface area and active surfaces, have attracted significant interest for use as anodes in LIBs/SIBs.[93,94] Among these, MXenes (with the general formula $M_{n+1}X_nT_x$, where M represents metals such as Cr, Mo, Zr,Ti, Nb, V…; X denotes C, N…; T_x indicates functional groups like –OH, –F, =O…; $n = 1$–4) have emerged as particularly promising anode materials due to their metal-like conductivity, adjustable interlayer spacing, and modifiable functional groups. $Ti_2NbC_2T_x$ is recognized as a representative double transition metal MXene.[95] However, akin to most 2D materials, MXene nanosheets tend to aggregate and self-stack, impeding electrolyte contact and severely constraining the effectiveness of active surfaces for redox reactions. This self-stacking phenomenon presents a major challenge in the development of MXene-based electrode materials.[75] Guo *et al.*[96] employed CA as the carbon source and EDA as the nitrogen source for the synthesis of nitrogen-doped carbon dots through a 5-hour hydrothermal treatment at 200 °C (Fig. 6a). Subsequently, they hydrothermally synthesized a typical double transition metal MXene, $Ti_2NbC_2T_x$, in conjunction with carbon dots, resulting in the formation of the $Ti_2NbC_2T_x$@CDs hybrid. XPS confirmed successful anchoring of the 0D carbon dots onto the surface/edge of 2D $Ti_2NbC_2T_x$ nanosheets through Ti(Nb)–O–C covalent bonds. Inductively coupled plasma emission spectroscopy analysis demonstrated a carbon dot loading of 16.8 wt%. The incorporation of CDs was found to weaken the interlayer force within $Ti_2NbC_2T_x$ nanosheets. Additionally, the formation of edge-crumpled $Ti_2NbC_2T_x$@CDs nanosheets modified surface terminations, effectively inhibiting the self-stacking of MXenes and increasing the exposure of reaction sites and terminal functional groups. This process further expanded the interlayer spacing, facilitating the rapid migration of Li^+ ions. Bader charge analysis indicated that, on

Table 2 Characterization methods and corresponding common characteristic data for BCDs

Characterization methods	Common characteristic data
TEM/SEM	BCDs exhibit excellent dispersibility, with particle sizes mostly smaller than 10 nm, and are predominantly spherical in shape
AFM	TEM can only determine the size on a two-dimensional plane and not the height of particles. When measuring the thickness of BCDs, it's typically found to be equivalent to several layers of graphene
HRTEM	The measurement of lattice fringe spacing typically falls within the range of 0.18–0.24 nm, although there are often instances where no distinct spacing is observed
XRD	Often, for amorphous carbon, the 2θ values range between 20 and 25, exhibiting broad diffraction peaks
FT-IR	BCDs typically contain chemical bonds such as –OH, C–H, C=O, and C=C, and other chemical functionalities. They may also include C–N and C–S bonds
XPS	BCDs typically contain carbon, oxygen, nitrogen, and sulfur, which can be reflected in XPS measurements. The spectra obtained from XPS can be used to determine the elements present in BCDs as well as the bonding modes between these elements. In BCDs, common bonds include C–C, C–N, C–O, C=O, and N–H
Raman	Defect-related D and G peaks are located near 1300 and 1580 cm^{-1}, respectively, with a 2D-peak ($\sim$2700 cm^{-1})
NMR	Nuclear Magnetic Resonance (NMR) carbon spectra can characterize the hybridization state of carbon in BCDs, typically showing a hybridization mixture of sp^2 and sp^3

average, the carbon atoms in CDs carried a positive charge, while the Li/Na atoms adsorbed onto the carbon layer also exhibited positive charges. This mutual repulsion contributed to a reduced diffusion barrier for Li/Na ions within the hybrid materials, enhancing ion diffusion kinetics. The pore structure of $Ti_2NbC_2T_x$@CDs hybrids was significantly enhanced compared to that of $Ti_2NbC_2T_x$. This enhancement was attributed to the prevention of self-stacking in MXenes due to their anchoring and intercalation by CDs. This process introduced micropores, mesopores, and wrinkles in the hybrid material, optimizing the pore size distribution and surface characteristics. Introducing 0D CDs into double transition metal MXenes led to a more stable discharge specific capacity for the $Ti_2NbC_2T_x$@CDs composite. This stability was observed after dynamic reorganization and reactivation of the material's framework, which was driven by rapid (de)intercalation of Li ions at high current density. As an anode, $Ti_2NbC_2T_x$@CDs exhibited a capacity of 217.3 mA h g^{-1} at a rate of 5 A g^{-1}, along with stable cycling performance and excellent capacity retention for lithium-ion batteries. Moreover, it demonstrated a remarkable capacity of 109.2 mA h g^{-1} at 5 A g^{-1} over 10 000 cycles for sodium-ion batteries.

The growth of lithium dendrites can lead to a series of issues such as low CE and safety threats in lithium-based batteries.[98–101] BCDs with designed functional groups can exhibit good dispersibility in organic electrolytes, and their abundant surface functional groups can synergistically combine with lithium ions. This synergistic combination facilitates uniform transportation of Li^+ to the current collector, leading to a smooth metal reduction on the surface during the plating and stripping process. Hong *et al.*[102] utilized CA as a carbon source and urea as a nitrogen doping agent to prepare UCDs (urea carbon dots) *via* a DMF solvent-thermal method. The carbon dots possess small sizes of 2–5 nm, ensuring good dispersibility in solvents. Elemental analysis (EA) and XPS measurements confirmed the presence of abundant carboxylic acid and pyridinic-N groups on their surfaces. These surface functional groups' unique combination of surface electrostatic attraction and strong affinity for lithium ions demonstrates significant potential in mitigating unstable lithium deposition. When utilized as an electrolyte additive, the diminutive size of the CDs initiates small initial Li nuclei, facilitating ideal Li stacking and the formation of a stable SEI. This unique advancement of the CDs was further explored through battery cycling tests. Li/Cu half-cell experiments utilizing the CDs exhibited the lowest overpotential, achieving an average CE of 95.5% over 100 cycles at cycling rates of 1 mA cm^{-2} and 1 mA h cm^{-2}. In contrast, tests without the CDs resulted in only 89.0% efficiency on average. Moreover, the CD-enhanced Li/Li symmetric-cell tests exhibited stable cycling for up to 500 cycles under conditions of 0.5 mA h cm^{-2} and 2.5 mA cm^{-2}. In stark comparison, the potential difference in pure Li/Li symmetric-cell tests significantly increased before completing 200 cycles. Furthermore, even under extreme testing conditions, such as a full-cell test with a $LiCoO_2$ cathode and a 20 μm Li metal anode, the inclusion of CD additives led to a remarkable average CE of 99.1% over 100 cycles and 99.9% capacity retention after this period (compared to 98.1% average CE and 57.9% capacity retention without CDs).

5.1.2 Lithium–sulfur batteries. Lithium–sulfur batteries have garnered significant attention for their low cost, high energy density (2600 W h kg^{-1}), and eco-friendliness.[103] However, the shuttle effect-where polysulfides generated during electrode reactions migrate between the cathode and anode-poses a significant challenge, leading to irreversible loss of active materials, hindering the practical application of lithium–sulfur batteries.[103,104] Strategies to address this issue typically involve loading sulfur into conductive host materials with high polysulfide adsorption capabilities.[105,106] In recent years, various high-performance host material/sulfur composite cathodes

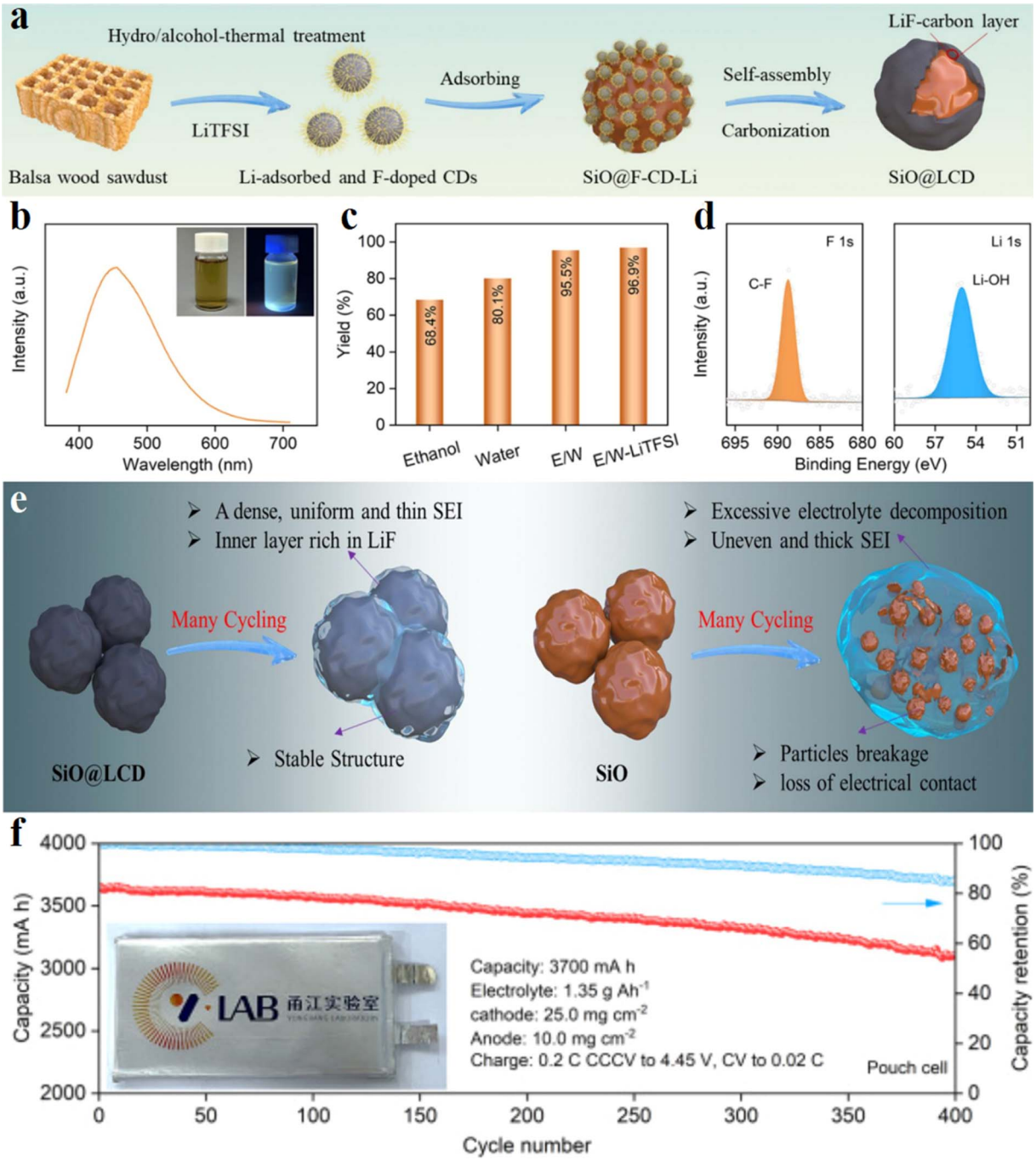

Fig. 5 Li-absorbed and F-doped carbon dots: (a) a schematic diagram depicting the synthesis process of F-CDs-Li and SiO@LCD; (b) PL spectra of F-CDs-Li solution (excitation at 365 nm) (insets showing digital images of the original F-CDs-Li solution and the solution under UV excitation); (c)the yield of CDs in various solvents; (d) the high-resolution F 1s and Li 1s spectra of F-CDs-Li; (e) schematic illustration of the influence of F-CDs-Li coating on the electrochemical performance of a SiO anode; (f) cycling stability of the pouch cell at 0.2C (1C = 3700 mA g^{-1}), with the inset showing the as-assembled pouch cell. Reproduced with permission.[44] Copyright 2023, Elsevier.

have been developed. However, the use of high surface area host materials for polysulfide adsorption requires excess electrolyte to prevent surface passivation, thereby impeding lithium-ion transport. Conversely, low surface area composites necessitate increased electrode thickness to achieve high sulfur content, resulting in an uneven electrolyte distribution. Consequently, in traditional strategies, the performance of host material/sulfur composite cathodes largely depends on the presence of excess electrolyte and low sulfur loading. Therefore, there is an urgent need to design host materials that allow for the preparation of sulfur cathodes under high sulfur loading and at low electrolyte-to-sulfur ratios (E/S). To achieve this goal, it is necessary to suppress the shuttle effect and ensure uniform electrolyte distribution in thick electrodes.[97] Previous studies have

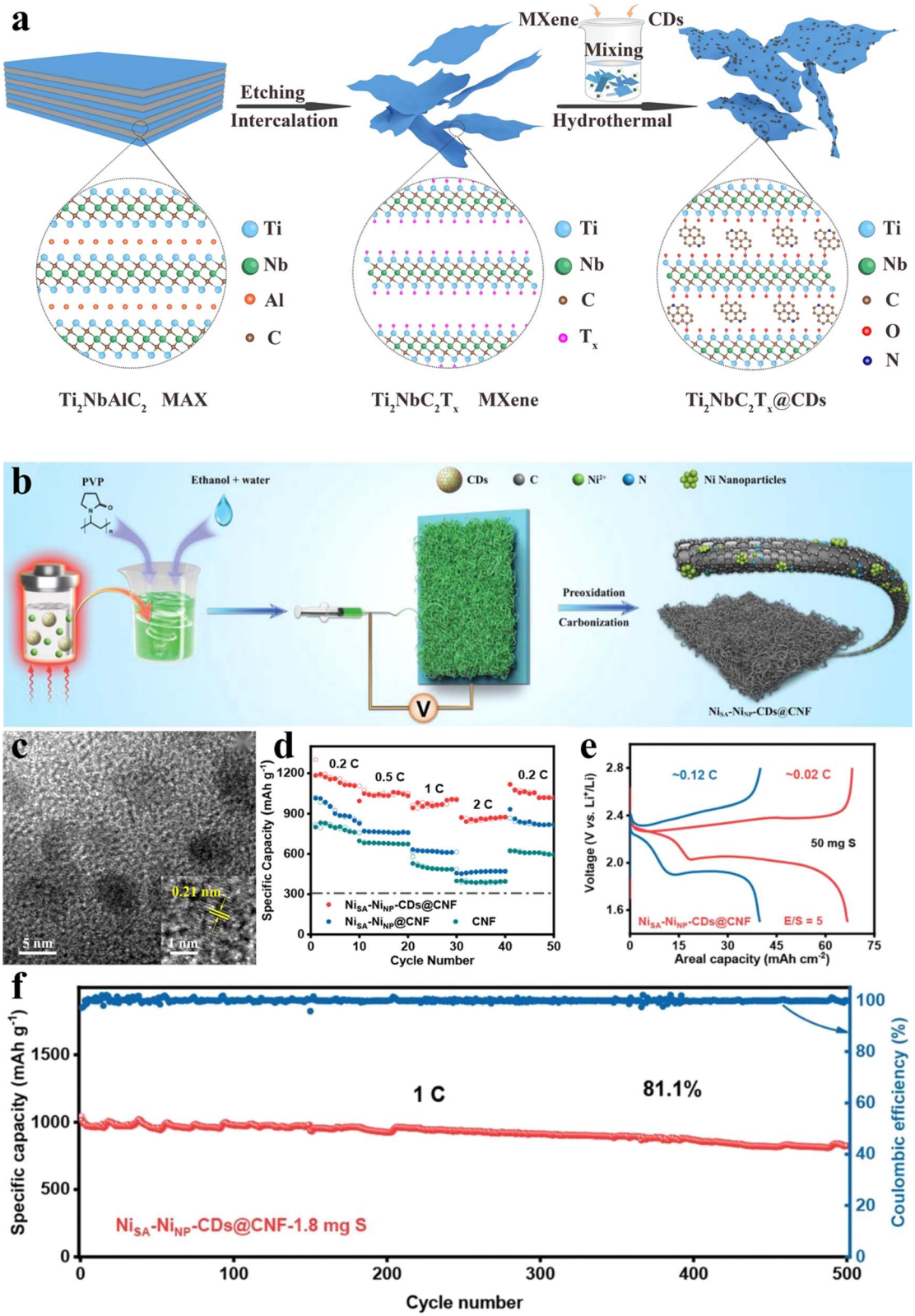

Fig. 6 Application of BCDs in lithium batteries: (a) a schematic diagram of the edge-crumpled $Ti_2NbC_2T_x$@CDs nanosheets; (b) schematic depiction of Ni_{SA}–Ni_{NP}-CDS@CNF; (c) TEM image of as-produced CDs of the $Ti_2NbC_2T_x$@CDs composite ((inset): HRTEM image of the CDs); (d) rate performance of different cathodes; (e) charge–discharge curves and (f) cycling stability of a sulfur cathode (sulfur loadings: 50 mg cm^{-2} and E/S: 5 μL mg^{-1}). (a and c) Reproduced with permission.[96] Copyright 2024, Elsevier. (b, d–f) Reproduced with permission.[97] Copyright 2022, Wiley-VCH.

indicated that a major factor contributing to the shuttle effect is the slow kinetic process of soluble polysulfide conversion to insoluble sulfides, followed by the migration of accumulated polysulfides driven by concentration diffusion and electric field effects.[107] Therefore, the shuttle effect can be mitigated by using catalytic host materials with low adsorption surface area that rapidly convert polysulfides.[108,109] Host materials with ordered porous 3D self-supporting structures facilitate electrolyte penetration. Among them, electrospun self-supporting carbon nanofibers (CNFs) are widely used due to their high conductivity, structural stability, and scalability.[110] However, the large pores and low specific surface area of CNFs may lead to aggregation and loss of loaded catalysts.[111] Lu *et al.*[97] employed carbon dots as aggregation inhibitors to fabricate self-supporting CNFs with nickel single-atom (Ni_{SA}) sites alongside small-sized, well-dispersed metallic nickel nanoparticles (Ni_{SA}–Ni_{NP}-CDS@CNF) as a scalable catalytic sulfur host, aiming to optimize both sulfur loading and the electrolyte-to-sulfur ratio (E/S) (Fig. 6b and c). A simple bottom-up hydrothermal approach was utilized, using CA as the carbon source and EDA as the nitrogen-doping agent, to synthesize nitrogen-doped carbon dots with an average diameter of approximately 4.7 nm at 200 °C for 5 hours. The XPS test confirmed the presence of abundant nitrogen- and oxygen-containing functional groups on the surface of the CDs. This structural feature allows the carbon dots' functional groups to adsorb metal ions, while the high temperature stability and crystalline cores of adjacent carbon dots act as spacers to prevent excessive metal migration, thereby providing more high-activity single-atom catalytic sites Ni_{SA}. As a result, Ni_{SA}–Ni_{NP}-CDS@CNF serves as a scalable sulfur host, allowing the sulfur cathode to achieve a high capacity of 66.5 mA h cm^{-2} at approximately 0.02C, along with impressive cycling stability (maintaining around 86.1% of its initial capacity after 100 cycles at approximately 0.12C), even at a low E/S of 5 μL mg^{-1} and a high sulfur loading of 50 mg cm^{-2} (Fig. 6d–f).

Liu *et al.*[112] employed egg white as the carbon source and synthesized N,S-CDs through self-doping of biomass materials. Ovalbumin and other components in the egg white freeze-dried powder can spontaneously adsorb onto Graphene Oxide (GO) nanosheets (Fig. 7a). Subsequently, after co-hydrothermal treatment at 250 °C for 12 hours and annealing under a nitrogen atmosphere at 800 °C for 2 hours, N and S co-doped CD decorated graphene composites (N,S-CDs/rGO) were obtained. The introduction of carbon dots imparts a three-dimensional porous structure to the material, while nitrogen and sulfur element doping from the carbon dots provides adsorption sites for polysulfides, thereby suppressing their diffusion. The N,S-CDs/rGO based cathodes exhibit superior performance characterized by higher rate capability and high sulfur utilization. Specifically, the N,S-CDs/rGO@S65 cathode (where 65 denotes the mass fraction of sulfur loading) demonstrates a capacity of 1550 mA h g^{-1} at a rate of 0.5C and maintains high capacities of 783.6 mA h g^{-1} at 5C, significantly outperforming rGO@S65. Remarkably, after 600 cycles of long-term cycling at 5C, the cathode retains a capacity of 427.9 mA h g^{-1} (Fig. 7b–d).

5.2 Sodium-ion batteries

The widespread use of lithium-ion batteries in various electronic devices has accelerated the consumption of lithium resources. It is foreseeable that the scarcity of lithium resources will hinder further development in the future. Sodium-ion batteries (SIBs), on the other hand, are seen as a potential supplement to LIBs due to the abundant reserves of sodium resources and their similar electrochemical mechanism to LIBs.[114] The strategy of using BCDs to modify battery materials is also applicable in sodium-ion batteries.

5.2.1 Anodes for sodium-ion batteries. Currently, one of the primary challenges in the field remains the lack of suitable anode materials exhibiting excellent sodium storage performance. Among various contenders, carbonaceous materials stand out for their promising attributes such as affordability, sustainability, structural robustness, and satisfactory performance, positioning them as potential candidates for commercial anodes in sodium-ion batteries (SIBs).[115,116] Nonetheless, their initial coulombic efficiency (ICE) still lags behind that of graphite anodes used in LIBs, posing a hurdle to widespread adoption. Although a scant number of literature studies have reported ICE values exceeding 90% for carbon materials in SIBs, this limitation significantly constrains energy density and hampers future commercial prospects.[117] Hence, the imperative lies in the development of high-performance carbonaceous anode materials with enhanced ICE, constituting a vital research avenue for the advancement of next-generation SIB technology.

Jensen *et al.*[113] subjected cellulose to hydrothermal treatment at 200 °C for 12 hours, obtaining cellulose-derived carbon dots (CCDs) from the supernatant of the reaction solution (Fig. 7e–g). TEM images of CCDs suggest that the CDs are some nanodomains with local graphitic nanostructures, embedded on the amorphous carbon layer during the HTC process. Subsequently, CCDs underwent further carbonization at 1300 °C for 1 hour in a nitrogen atmosphere, resulting in CCD1300. Similarly, solid contents from the deposit in the reaction solution were subjected to the same procedure to obtain cellulose-derived HTC carbons (CHTCs). The XPS survey (Fig. 7h) and fitted C 1s peaks reveal that carbonized CHTCs have a substantially higher oxygen content compared to CCDs, suggesting the presence of more topological defects. This lower oxygen content in CCDs could potentially be a result of the highly ordered nanodomains, which facilitate oxygen decomposition during the carbonization process, thereby allowing carbon atoms in the surrounding to diffuse towards the graphitic domains and form ordered microstructures. CCD1300 exhibits a significantly improved Initial Coulombic Efficiency (ICE) along with outstanding sodium storage capacity, attributed to its lower surface area, reduced defect density, and higher degree of graphitization. Notably, CCD1300 demonstrates an impressive ICE of 91%, which ranks among the highest values reported for hard carbon anodes in SIBs (Fig. 7i). This enhancement can be linked to the condensed stacking morphology and reduced specific surface area of the CCD samples, which minimize the contact area between the electrolyte and electrode, thus

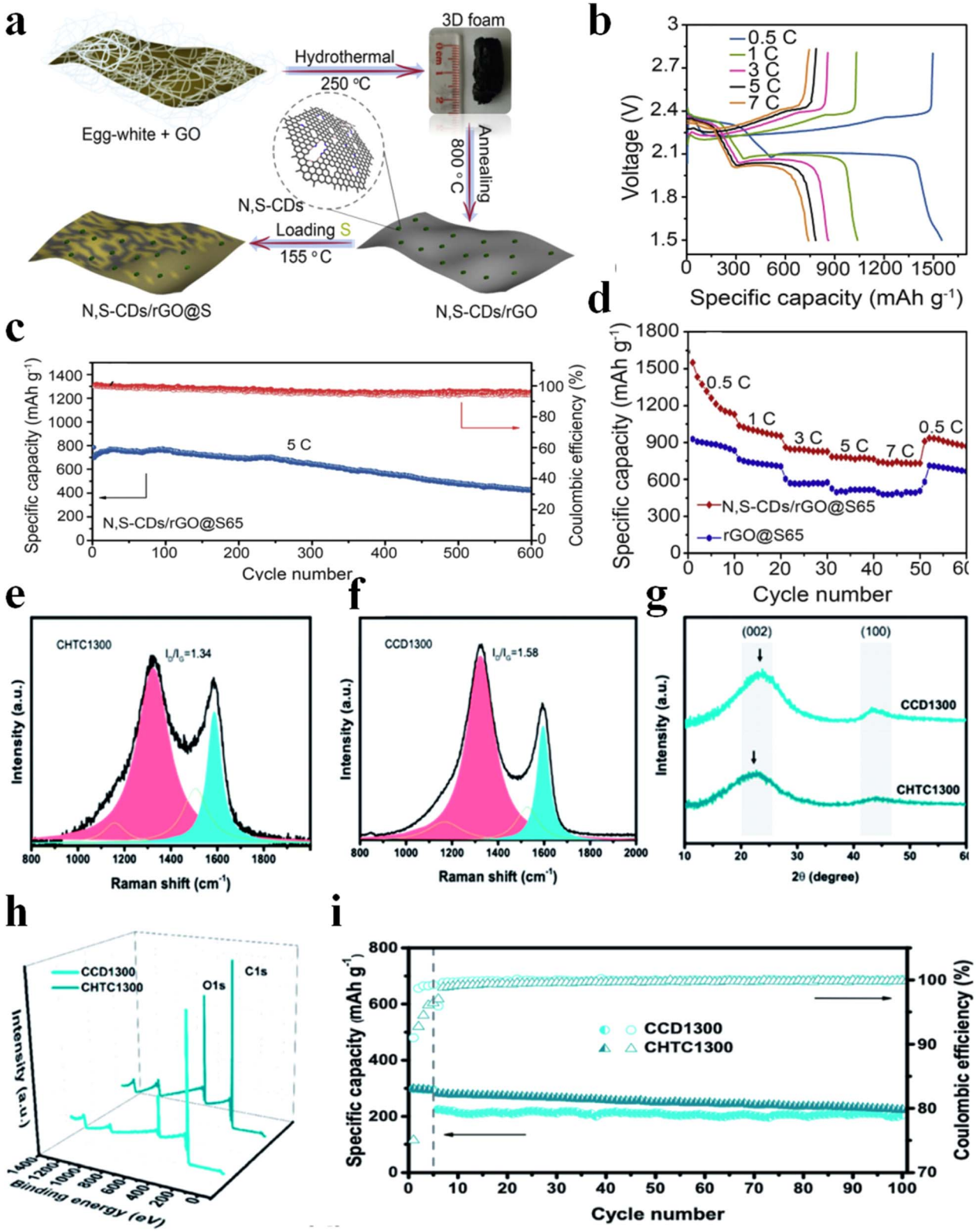

Fig. 7 CDs from egg white and cellulose: (a) a schematic diagram depicting the fabrication process of the N,S-CDs/rGO@S composites; (b) the charge/discharge profiles of N,S-CDs/rGO@S65 at various rates; (c) long-term cycling stability of N,S-CDs/rGO@S65 at 5C for 600 cycles; (d) rate performance comparison between N,S-CDs/rGO@S65 and rGO@S65; (a–d) reproduced with permission.[112] Copyright 2019, Elsevier. (e) Raman spectra of CHTC1300 and (f) CCD1300; (g) XRD patterns; (h) XPS survey; (i) cycling stability of CCD1300 and CHTC1300 in half cells at a current rate of 150 mA g^{-1} (with the initial five cycles conducted at 30 mA g^{-1}). (e–i) Reproduced with permission.[113] Copyright 2019, Royal Society of Chemistry.

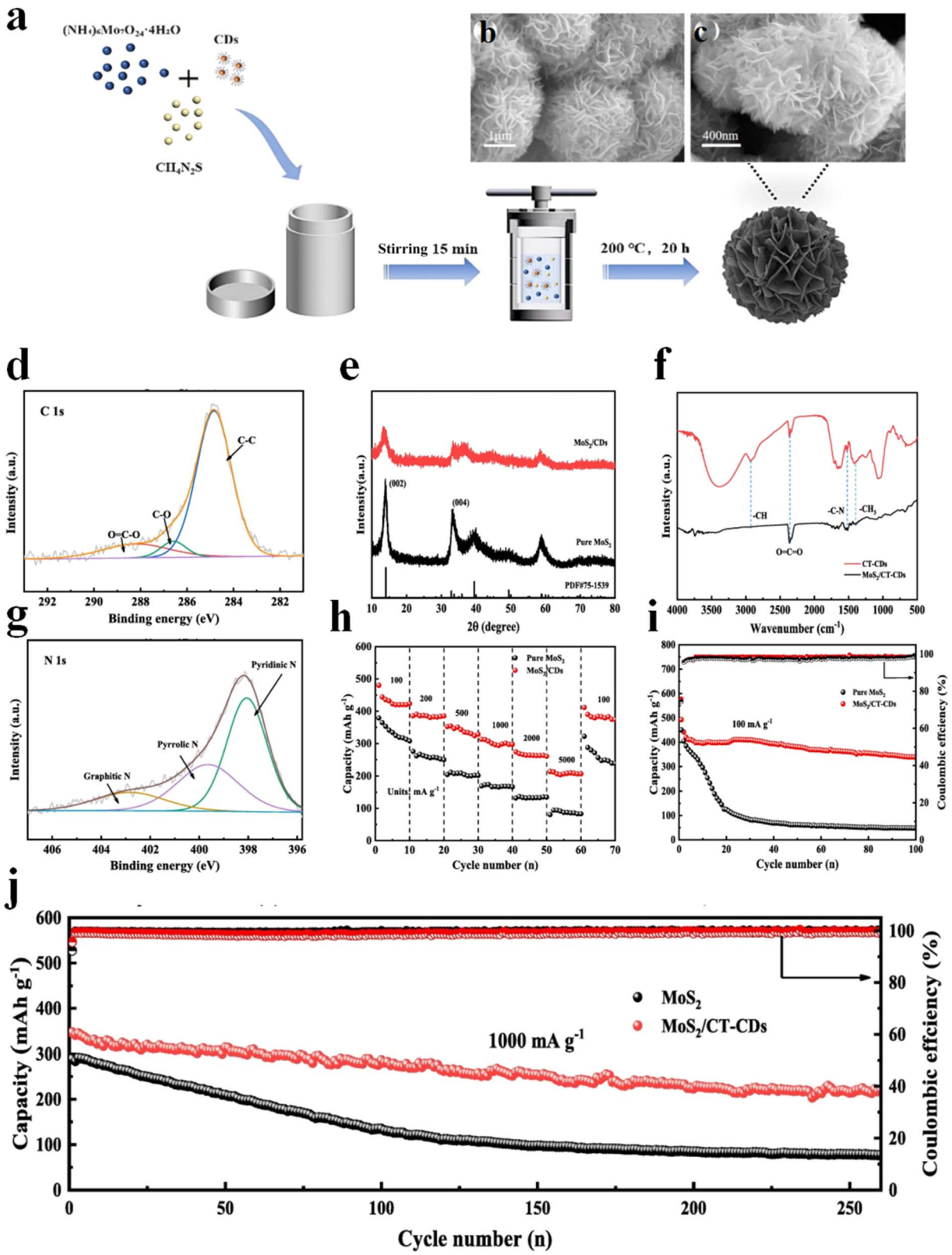

Fig. 8 CT-CDs derived from chitin: (a) schematic illustration of the synthesis process of MoS_2/CT-CDs; (b and c) SEM images of MoS_2/CT-CDs; (d) C 1s XPS spectrum; (e) XRD pattern; (f) FT-IR spectrum; (g) N 1s XPS spectrum; (h) rate properties of MoS_2 and MoS_2/CT-CDs; (i) cycle properties of MoS_2 and MoS_2/CT-CDs; (j) long-term cycle stability of MoS_2 and MoS_2/CT-CD. Reproduced with permission.[55] Copyright 2024, Elsevier.

facilitating the formation of a less SEI. Additionally, the more ordered nanostructure, lower concentration of oxygen functional groups, and reduced defect density result in fewer sodium ions being trapped with high binding energy, thereby reducing irreversibility in the first cycle.

Metal sulfides possess significant theoretical specific capacities and energy densities, rendering them excellent candidates for anodes in sodium-ion batteries. MoS_2, with its graphene-like layered architecture and weak van der Waals forces between the layers, facilitates efficient pathways for Na^+ ion intercalation/deintercalation. The theoretical sodium storage capacity of MoS_2 can reach 600 mA h g^{-1}.[118] Nevertheless, its low intrinsic conductivity hinders the effective transfer of ions and electrons. Additionally, MoS_2 experiences volumetric expansion during charge and discharge cycles, leading to electrode material deformation.[119] Carbon materials, known for their high conductivity and ability to facilitate rapid charge transfer while reducing agglomeration, have been utilized to improve the sodium storage capabilities of MoS_2.[120,121] Wang *et al.*[55] utilized chitin as a carbon and nitrogen source to prepare 10 nm sphere-like carbon dots (CT-CDs) *via* the hydrothermal method (Fig. 8a–c). XPS analysis reveals that CT-CDs contain abundant nitrogen- and oxygen-containing functional groups, which can create various surface defects and generate additional active sites (Fig. 8d–g). These CT-CDs served as functional structural inducers, facilitating the assembly of MoS_2 nanosheets into MoS_2/CT-CDs nanocomposites that exhibited hydrangea-like structures. In contrast to the original block-like configuration of MoS_2, the hydrangea-like morphology, combined with the increased spacing between layers, offered additional active sites and pore channels, which promoted the adsorption and transport of sodium ions, notably improving the electrochemical reaction kinetics. The MoS_2/CT-CDs, synthesized *via* CT-CD induction, demonstrated reduced impedance while mitigating electrode material failure due to agglomeration and fragmentation, thereby accommodating volume changes during battery operation and improving long-term cycling stability. When utilized as the anode in sodium-ion batteries, MoS_2/CT-CDs achieved a high reversible capacity (338.9 mA h g^{-1}, at 0.1 A g^{-1}, after 100 cycles and 219.9 mA h g^{-1}, at 1 A g^{-1}, after 260 cycles) (Fig. 8h–j).

Transition metal sulfides have emerged as among the top electrode materials for SIBs because of their impressive theoretical capacity and the presence of numerous active sites.[122] Furthermore, mixed metal sulfides have garnered increasing attention in the field of energy storage compared to single-metal sulfides. This is attributed to their capacity to produce synergistic effects, lower band gaps, and enhanced conductivity.[123] For instance, the $Ni_xCo_{3-x}S_4$ compound demonstrates a wider range of redox reactions and greater specific capacitance than its individual single-metal sulfides (NiS_x/CoS_x).[124] Nevertheless, the cycling stability and rate performance of $Ni_xCo_{3-x}S_4$ are hampered by volumetric expansion that occurs during the redox process. The introduction of a highly conductive and buffering matrix, such as carbon materials, is regarded as an effective strategy, to mitigate volume expansion and prevent self-aggregation, ultimately improving the cycling stability of the electrode material.[125,126] Fan *et al.*[51] utilized glucose as the carbon source and conducted a reaction at 200 °C under a nitrogen atmosphere for three hours to produce carbon dots (Fig. 9a). The HRTEM images of the CDs reveal their size range to be below 10 nm, and demonstrate a lattice spacing of 0.21 nm, which matches well with the (100) plane of graphite carbon (Fig. 9c and d). In contrast to conventional methods where carbon dots are synthesized first and then applied to materials, this study initially synthesized nickel–cobalt bimetallic sulfide $NiCo_2S_4$, which possesses abundant internal pores. Subsequently, the carbon source glucose was loaded into these internal pores and carbonized. The finally formed $NiCo_2S_4$@-CDs, resulting from the synergistic interactions of Co/Ni-based bimetallic sulfides, the confinement provided by carbon dots, and the distinctive cross-stacked structure, shows a greater discharge specific capacity than pure $NiCo_2S_4$. The carbon dot-based conductive network enhances electrical conductivity, allowing for efficient transport of electrons/Na^+. Additionally, the introduction of CDs effectively suppresses volume expansion and self-aggregation of the electrode material, thereby improving cycling life. When used as anodes in SIBs, $NiCo_2S_4$@CDs achieved a rate capacity of 568.9 mA h g^{-1} at 0.5 A g^{-1} and maintained a discharge specific capacity of 302.7 mA h g^{-1} after 750 cycles at 5.0 A g^{-1} (Fig. 9g).

5.2.2 Cathodes for sodium-ion batteries. Sodium-ion batteries require high energy density and fast charging, but the charge transfer kinetics of cathode materials limit their performance.[128,129] Currently, strategies such as using carbon composites and structural engineering have been employed to improve the performance of cathode materials.[130–133] However, challenges still exist, including the competition between conductivity and electrochemical activity, as well as the optimization of interface structures.[134]

Bai *et al.*[127] employed diethylenetriamine as a dopant and tartaric acid as a carbon source to synthesize nitrogen-doped CDs through a 30-minute stirring heating process at 130 °C in an ethanol solution. Subsequently, the carbon dots, in a facile co-precipitation method, acted as an ionic surfactant to control the particle-growth process of the sodium-ion cathode material NASICON (Sodium Super Ionic Conductor) structured polyanion $Na_3V_2(PO_4)_3$ (NVP) (Fig. 9b and e). The incorporated carbon dots, featuring a wealth of surface functional groups (–NH_2 and –OH) and a ζ potential of 4.54 mV, were firmly anchored to the surface of NVP, effectively halting further growth of NVP crystals (resulting in a slight increase in specific surface area from 2.5 to 17.5 m^2 g^{-1}). This shortened the ion-diffusion path, thereby accelerating diffusion kinetics. Furthermore, compared to conventional carbon composites with high carbon contents, the electrical conductivity of NVP was markedly enhanced through the incorporation of trace amounts of carbon (0.76 wt%) (Fig. 9f), effectively striking a balance between electrical conductivity and electrochemical performance of NVP. Moreover, the incorporated CDs with plentiful functional groups (–NH_2 and –OH) (Fig. 9j–l) facilitated the rapid decomposition of $NaPF_6$ and accelerated NaF deposition kinetics on the NVP surface, resulting in the formation of a thin and stable NaF-rich cathode-electrolyte

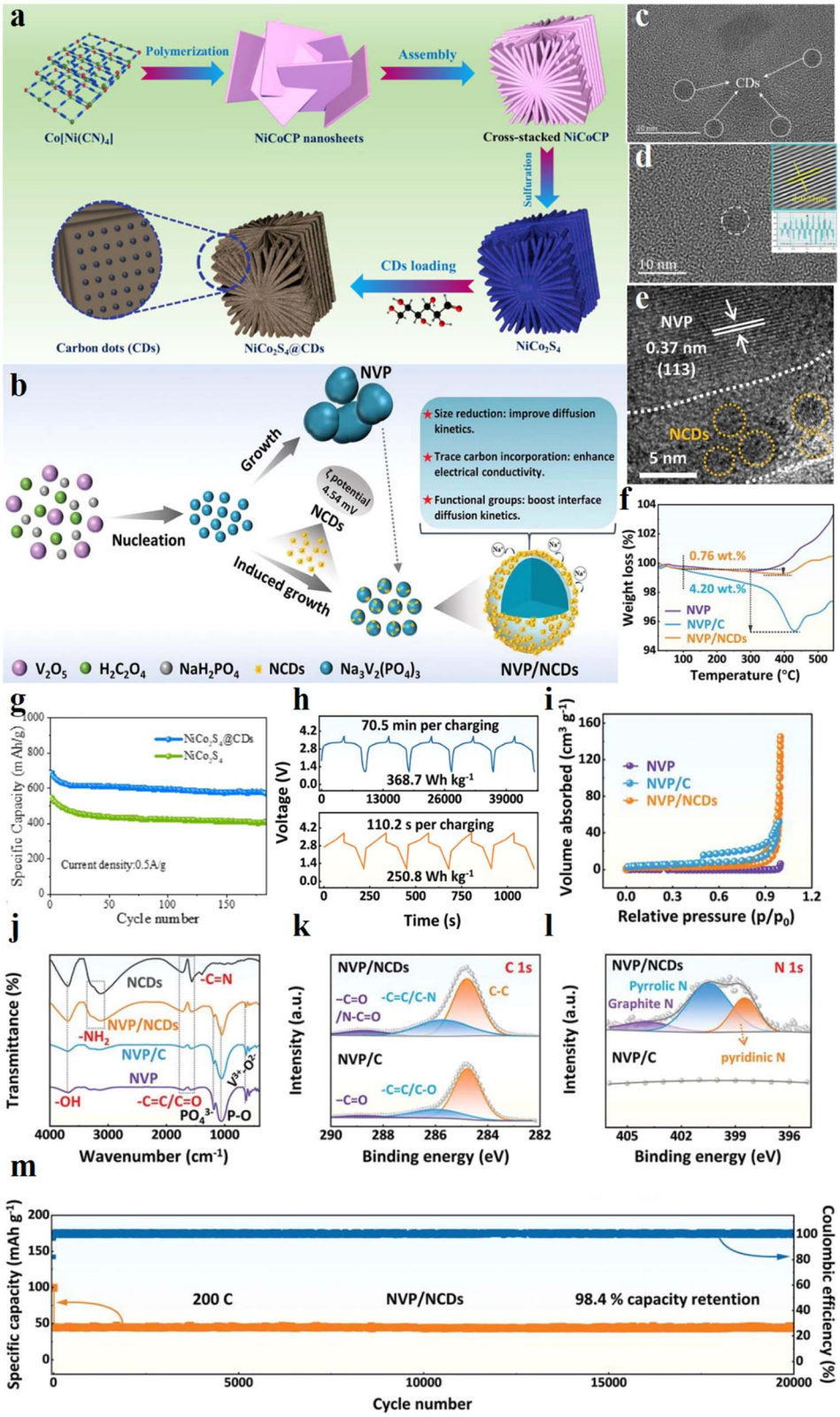

Fig. 9 BCDs derived from glucose and tartaric acid: (a) schematic illustration of synthesis of $NiCo_2S_4$@CDs through the assembly of nanosheets into a cross-stacked superstructure, followed by the incorporation of CDs; (b) diagram illustrating the optimization mechanism for the integration of CDs into NVP; (c and d) HRTEM image of the carbon dots in $NiCo_2S_4$@CDs, with the inset in (d) displaying the inverse FFT patterns; (e) STEM of NVP/NCDs (f) TGA; (g) cycle performance of $NiCo_2S_4$@CDs and $NiCo_2S_4$ in SIBs; (h) dQ/dV curves for the NVP/NCDs cathode and hard carbon anode in a full cell; (i) N_2 adsorption–desorption isotherm; (j) FT-IR spectra and (k) C 1s spectra; (l) N 1s spectra; (m) cycling performance of NVP/NCDs. (a, c, d and g) Reproduced with permission.[51] Copyright 2023, Elsevier. (b, e, f, h–m) Reproduced with permission.[127] Copyright 2024, Wiley-VCH.

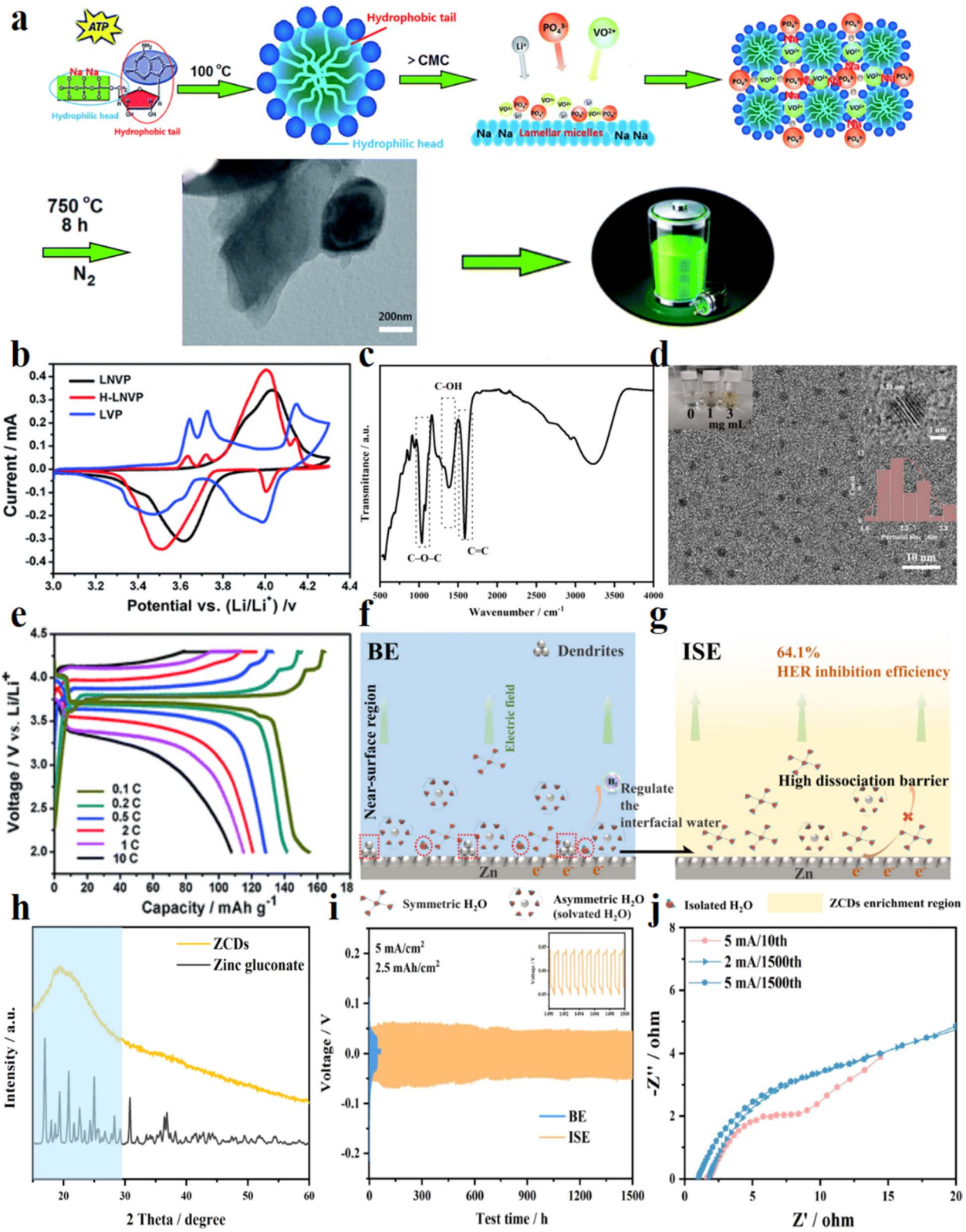

Fig. 10 BCDs derived from ATP and zinc gluconate: (a) schematic representation of the synthesis process of H-LNVP nanocomposites; (b) the cyclic voltammograms of pure LVP, LNVP and H-LNVP at 0.1 mV s^{-1}; (c) FT-IR spectra of ZCDs; (d) TEM images of ZCDs, the inset image (left) shows the physical image of electrolytes with different concentrations of ZCDs placed for five months; (e) initial charge–discharge profiles of H-LNVP at different rates; schematic illustrations of interfacial reactions of the Zn anode in (f) conventional Zn^{2+} electrolyte and (g) functional Zn^{2+} electrolyte containing ZCDs; BE: benchmark $ZnSO_4$ electrolyte; ISE: inorganic nanoparticle suspension electrolyte; (h) XRD patterns; (i) long-term cycling performance of symmetric Zn||Zn cells; (j) electrochemical impedance spectra. (a, b and e) Reproduced with permission.[135] Copyright 2017, Royal Society of Chemistry. (c, d, f–j) Reproduced with permission.[136] Copyright 2023, Elsevier.

interface layer. This significantly improved the interfacial sodium-ion diffusion kinetics. Consequently, the carbon dots conferred ultrastable cyclability to $Na_3V_2(PO_4)_3$, with a retention of 98.4% capacity over 20 000 cycles in a half cell, as well as excellent rate capability (up to 200C). Additionally, in a full cell configuration, the material exhibited fast charging properties (approximately 110.2 s per charging with 250.8 W h kg^{-1} input) and high energy density (368.7 W h kg^{-1}) (Fig. 9h and m).

Zhang *et al.*[135] utilized the biomolecule, ATP, as the anionic surfactant and biocarbon to synthesize the layered hybrid phase $Li_2NaV_2(PO_4)_3$/carbon dot (H-LNVP/CD) nanocomposite through sol–gel and carbon thermal reduction methods (Fig. 10a). This novel composite cathode demonstrated a reversible capacity of 158 mA h g^{-1} at 0.1C in a mixed-ion cell containing Li^+/Na^+, facilitated by the electrochemically active redox reactions of V^{4+}/V^{5+} and V^{3+}/V^{4+} (Fig. 10b), significantly surpassing single-phase contrastive samples. The battery exhibited a prominent high voltage plateau, featuring a distinct discharge voltage at around 3.7 V, along with a CE of approximately 100% at 10C (Fig. 10e). These performances were partly credited to the CDs on the surface of layered H-LNVP nanoparticles, which significantly enhanced their electronic conductivity. The high-energy biomolecules produced CDs (average size of about 3 nm) on the surface of the layered structure through the thermal decomposition reduction method. Due to the high surface-to-mass ratio of CDs, a greater number of lithium ions could be accommodated on the sites. Leveraging the remarkable physical properties of CDs such as the quantum tunneling effect and high electron mobility, the transport efficiency of Li^+ ions and electrons was increased.

5.3 Zinc ion batteries

With the development of renewable energy and the expansion of the electric vehicle market, there is a continuous increase in demand for high-performance, high-safety batteries.[137] Zinc-ion batteries have attracted attention due to their low cost,[138] high safety,[139] and environmental friendliness.[140] However, their practical application is limited by various issues that occur with the zinc anode during the cycling processes, such as zinc dendrite growth,[141] parasitic reactions,[142] and electrode surface corrosion.[143] The poor electrical conductivity and structural stability of the cathode also result in slow reaction kinetics and weak cycling durability.[144] Biomass-derived carbon dots, as highly cost-effective modifiers, find applications in various components such as zinc electrolytes, cathodes, and separators in zinc batteries.

5.3.1 Electrolyte additives. Peng *et al.*[136] conducted a thermal decomposition of zinc gluconate in an argon atmosphere at 160 °C for 2 hours. Following this, the resulting product was dissolved in water, filtered to eliminate large particles, and then purified through dialysis and freeze-drying to yield zinc-doped CQDs (ZCDs) (Fig. 10d). The presence of Zn^{2+} ions prevents uncontrolled aggregation during the pyrolysis process and they serves as passivation agent for surface defects. These carbon dots display a uniform quasi-spherical morphology with an average diameter measuring 2.24 nm. FT-IR (Fig. 10c) and XPS confirmed the presence of oxygen-containing functional groups such as hydroxyl and carboxyl groups on the surface of ZCDs. These functional groups not only ensure good dispersibility of the carbon dots in the electrolyte but also interact with water molecules, dynamically enriching at the zinc/water interface and regulating the structure of the interface water (Fig. 10f and g). By controlling the structure of the interface water, the number of solvated water molecules is reduced, thereby decreasing electrochemical reactions at the interface. This promotes a uniform plating/stripping process for zinc. Consequently, the Zn anode shows predominantly dendrite-free plating and stripping behavior when in contact with this distinctive electrolyte, a remarkable 64.1% inhibition efficiency against the hydrogen evolution reaction, a significantly prolonged cycle life (over 1500 hours at 5 mA cm^{-2}), an outstanding cumulative capacity of approximately 3.75 A h cm^{-2}, and a capacity retention of around 83% in a $Zn\|V_2O_5$ battery over 4000 cycles (Fig. 10i and j).

Zhang *et al.*[5] synthesized blue-fluorescent carbon dots (B-CDs) rich in zinc-binding groups using CA and EDA as carbon and nitrogen sources, respectively, *via* a microwave-assisted method (Fig. 11a–c). The B-CDs exhibit a consistent dispersion (average diameter of around 2.3 nm), as evidenced by the TEM image. Moreover, the HRTEM images indicate that the CDs possess high crystallinity, featuring a lattice spacing of 0.21 nm, which aligns closely with the *d*-spacing of the graphene (100) plane (Fig. 11d). Through thorough examination of Raman and XRD spectra, the presence of sp^2 and sp^3 hybridization further underscores the high degree of crystallization and graphitization of B-CDs. Additionally, the FT-IR spectra reveal characteristic vibrations corresponding to –OH, $–NH_2$, –CN, –COOH, and –CO, which are in close agreement with the XPS results (Fig. 11e). Notably, B-CDs exhibit a consistent spatial distribution in a 2 M $ZnSO_4$ solution with a lower ζ potential. This, coupled with the abundance of functional groups on their surface and their stable presence in the aqueous $ZnSO_4$ electrolyte, positions them as viable additives for stabilizing Zn anodes. Experimental and computational simulations corroborate the effectiveness of an ultrathin Zn^{2+} adsorbing layer composed of carbon dots with zincophilic groups on the surface of the Zn metal. This layer optimizes the distribution of the electric field, reduces nucleation energy barriers, and enhances anticorrosion currents. It's worth noting that the presence of B-CDs in the electrolyte leads to a higher nucleation energy barrier for the Zn electrode (39.5 mV), ascribed to the deposition of B-CDs alongside Zn^{2+}. Furthermore, the increased nucleation overpotential in electrolyte with B-CDs facilitates the formation of smaller Zn grains with an advantageous crystallographic orientation. With the CDs providing protection, the Zn anode successfully achieved extended Zn plating/stripping with a reduced voltage hysteresis of 37 mV (at a current density of 1 mA cm^{-2} for 2500 h). This study presents another innovative aspect wherein carbon dots not only function as effective inhibitors for zinc dendrites but also capitalize on their fluorescence properties. The carbon core, featuring a rich array of peripheral structures, induces intense blue fluorescence from B-CDs (Fig. 11f–h). Utilizing fluorescent carbon dots as a color

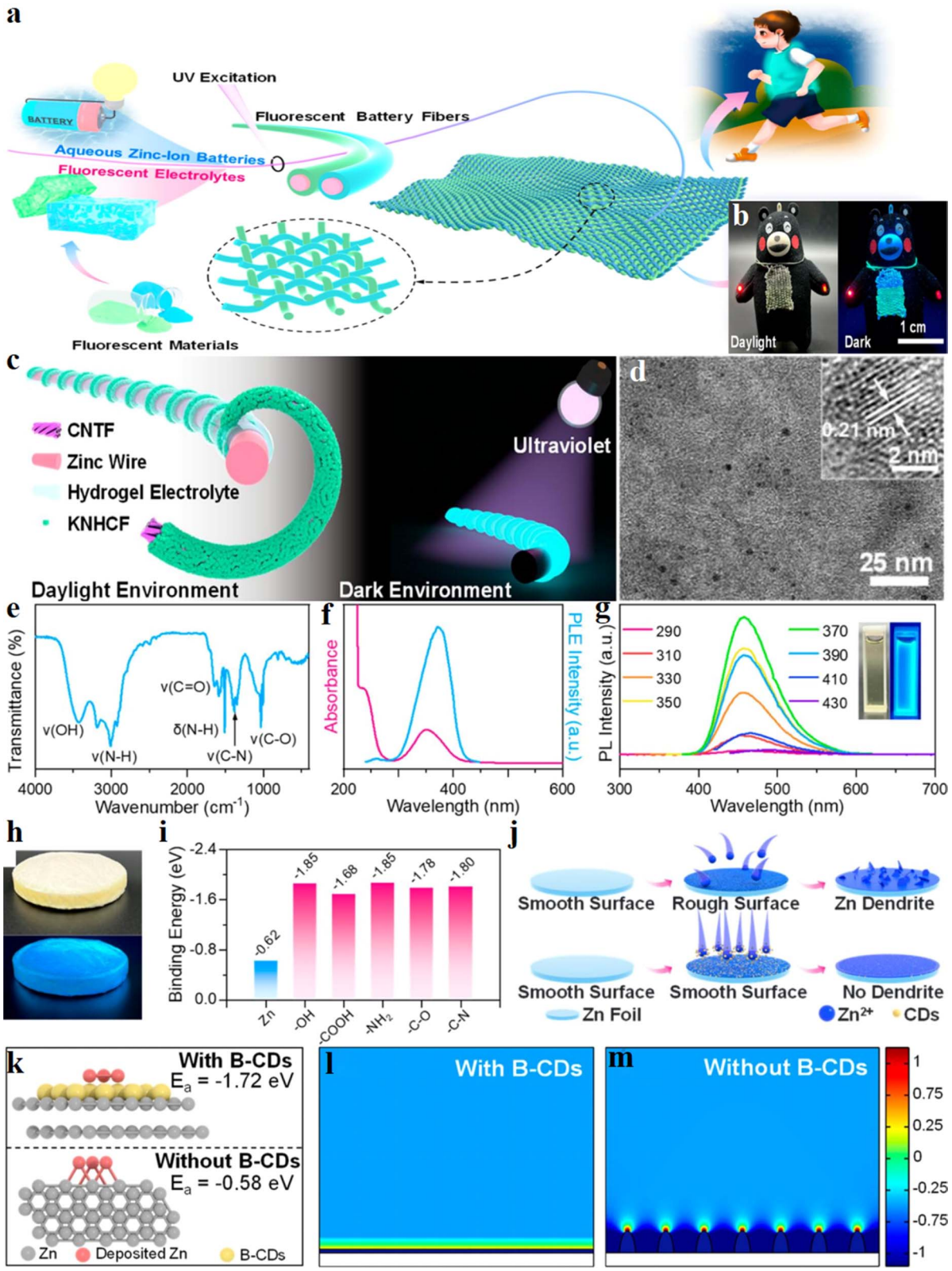

Fig. 11 Blue-fluorescent carbon dots: (a) diagram illustrating a display-integrated battery textile made from FFAZIBs; (b) images of the display-integrated battery under sunlight, alongside photographs of a LED powered by the textile, shown in daylight and a dark setting under 365 nm excitation; (c) diagram of the all-solid-state FFAZIB; (d) TEM image of B-CDs, inset shows the HRTEM image; (e) FT-IR spectra of B-CDs; (f) absorption and photoluminescence excitation spectra of B-CDs; (g) emission spectra of B-CDs, with the inset showing B-CDs in water under sunlight and a UV lamp; (h) images of B-CDs embedded in a PVA hydrogel in the solid form under sunlight and a UV lamp; (i) bar chart displaying binding energies of Zn atoms to different functional groups; (j) diagram illustrating the role of B-CDs in reducing Zn dendrite growth; (k) Zn adsorption on the Zn surface; electric field distribution of a Zn electrode (l) with B-CDs and (m) without B-CDs. Reproduced with permission.[5] Copyright 2023, American Chemical Society.

filter, they are introduced into electrolytes to fabricate fluorescent fiber-shaped aqueous zinc-ion batteries (FFAZIBs). This serves as a proof-of-concept design for integrating displays into battery fibers for multifunctional smart textiles (Fig. 11i–m). Additionally, a prototype FFAZIB with a high voltage plateau (1.55 V) was successfully fabricated by encasing a zinc wire with free-standing Prussian blue, pre-coated with a fluorescent gel electrolyte. These resulting FFAZIBs leverage the protective benefits provided by electrolyte additive engineering for the zinc anode, along with the multiple active sites available in the free-standing Prussian blue cathode. This combination enables exceptional cyclability (with a capacity retention of 78.9% after 1500 cycles) and a high energy density of 0.17 W h cm^{-3}. It's worth noting that the hydrophilic groups of carbon dots can provide poly(vinyl alcohol) (PVA) hydrogel electrolyte with robust water retention capacity. In contrast to electrolytes lacking B-CDs, those incorporating B-CDs are able to maintain 78% of their moisture content after being exposed to ambient conditions for 10 days. The inevitable aggregation of fluorophores of carbon dots leads to aggregation-caused quenching (ACQ), resulting in the disappearance of fluorescence in the solid state. Fortunately, ACQ can also be effectively mitigated by the PVA hydrogel, which markedly reduces the interaction between B-CDs and increases their separation. This ultimately maintains good stability and blue fluorescence in the solid state.

5.3.2 Separators. Traditional separators, such as glass fiber (GF)[145] and cotton fiber filter paper, encounter challenges like low ion conductivity and uneven pore distribution.[146] Despite being an economically viable choice, cellulose filter paper (CF) still grapples with issues arising from its large and uneven pore structure, obstructing ion transport and leading to uncontrolled zinc dendrite growth. These constraints significantly impede the further advancement of AZIB technology.

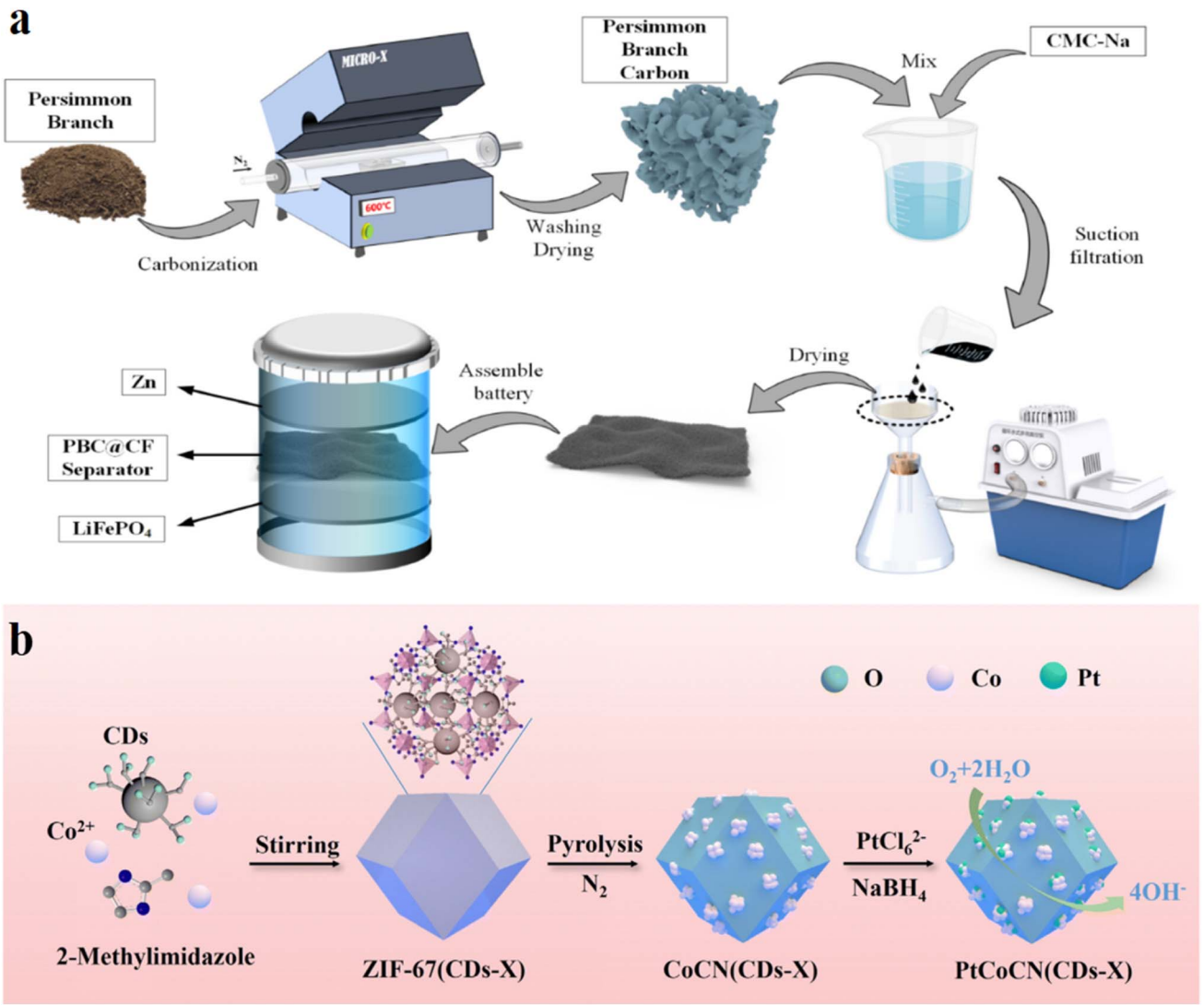

Fig. 12 (a) Schematic illustration depicting the preparation process of PBC@CF-separators and their application in an aqueous Zn–$LiFePO_4$ dual ion full battery; Reproduced with permission.[147] Copyright 2022, Elsevier. (b) Schematic diagram of the formation of the PtCoCN (CDs-X) catalyst. Reproduced with permission.[148] Copyright 2024, Royal Society of Chemistry.

Yu *et al.*[147] subjected persimmon branches to drying at 120 °C for 12 hours followed by carbonization at 600 °C for 2 hours under a nitrogen atmosphere, yielding persimmon branch carbon (PBC) embedded with evenly dispersed CDs (Fig. 12a). Subsequently, they utilized a cellulose filter paper separator modified with PBC to obtain an efficient ion transport modulator, the PBC@CF separator. TEM analysis revealed that PBC displayed a porous structure with uniformly sized carbon dots ranging from 3 to 5 nm. XPS measurements indicated that its surface possessed abundant functional groups containing N and O, enhancing the separator's wettability and zincophilicity. O and N atoms in PBC repelled SO_4^{2-}, thereby limiting anion migration and promoting cation transference, ultimately resulting in a high Zn-ion transport rate. Additionally, the irregular macropores in the CF separator were filled with PBC particles, resulting in a more uniform interface layer that functions as an ion redistribution device, thereby ensuring an even distribution of the electric field at the separator-anode interface. The ionic conductivity of the modified PBC@CF separator was improved, increasing from 8.85 to 17.63 mS cm^{-1}. Additionally, the zinc nucleation overpotential was reduced, while the exchange current density increased from 4.78×10^{-2} to 7.32×10^{-2} mA cm^{-2}, while also improving the reversibility of zinc stripping and plating when compared to those of the CF separator. The zinc symmetrical cell utilizing the PBC@CF separator exhibited stable cycling over 300 hours at 1 mA cm^{-2}, approximately three times higher than the performance of the cell with the CF separator. Additionally, the Zn–$LiFePO_4$ dual-ion full battery with the PBC@CF separator demonstrated excellent rate capability and remarkably enhanced cycling stability over 200 cycles, maintaining 86% of its initial capacity at 1C compared to batteries utilizing the CF separator.

5.3.3 Cathodes for zinc ion batteries. V_2O_5, as a low-cost,[149] high-capacity cathode material,[150] holds great potential for various applications. However, its performance is still not ideal due to issues such as poor structural stability during cycling and slow ion diffusion kinetics.[149,151] Zheng *et al.*[152] first subjected chitosan to ultrasonic treatment, followed by a 12-hour hydrothermal process at 180 °C, resulting in the synthesis of monodisperse nitrogen-doped carbon dots (particle size of 3.08 nm and lattice spacing of 0.21 nm) (Fig. 13a). XPS and FT-IR analyses confirmed the presence of abundant N-functional groups on the surface (Fig. 13b–d). Subsequently, chitosan carbon dots (CCDs) were incorporated into V_2O_5 using a straightforward hydrothermal process, yielding CCDs@V_2O_5 nanobelts characterized by a distinctive one-dimensional structure and exceptional electrochemical properties. The mass fraction of CCDs within the nanobelts was determined to be 7.92 wt% (Fig. 13e). The nitrogen-doped oxygen vacancies in the carbon dots were found to weaken the interaction between zinc ions and the main structure, thereby facilitating Zn^{2+} diffusion. Furthermore, these vacancies contributed to the formation of V^{4+} species. Additionally, the larger ion radius of V^{4+} in the coordination bond, compared to V^{5+}, promoted lattice spacing expansion, enhancing the reversibility of Zn^{2+} insertion and extraction (Fig. 13g–i). The incorporation of CCDs expanded the specific surface area of V_2O_5, thereby improving the interface contact between the electrode and electrolyte (Fig. 13f), and consequently shortening the diffusion path length for zinc ions. Moreover, the unique one-dimensional structure of the nanobelts provided additional pathways for electron transfer, thereby accelerating the kinetics of diffusion reactions (Fig. 13j). The CCDs@V_2O_5 nanobelts exhibit significant potential as a cathode for AZIBs. They demonstrated outstanding rate performance and impressive long-term cycling stability. The battery achieves a specific capacity of 401.4 mA h g^{-1} at 0.1 A g^{-1}, and the specific capacity remains high at 285.3 mA h g^{-1} even after 400 cycles at 1 A g^{-1}. Remarkably, the specific capacity still reaches 212.30 mA h g^{-1} after enduring 2000 cycles at 4 A g^{-1}, retaining an impressive capacity retention rate of 83.77%.

Zhang *et al.*[153] employed glucose as a carbon source, and treated it with V_2O_5 under hydrothermal conditions at 140 °C for 24 hours to construct conductive CQD decorated V_2O_5 nanobelts. From the HRTEM image, it is evident that the carbon dots, with an approximate diameter of 3 nm, are uniformly dispersed within the V_2O_5 framework. Through thermogravimetric analysis (TGA), the mass fraction of CDs in the composite material was determined to be 4.26 wt%. XPS results reveal the partial reduction of some V^{5+} ions to V^{4+}. The presence of the mixed valence states of V^{4+} and V^{5+} allows for the possibility of a multi-electron reaction during zinc intercalation/deintercalation. The V_2O_5/CQDs nanobelts exhibit a BET surface area of 9.4 m^2 g^{-1}, double that of unmodified V_2O_5. This increased surface area is anticipated to bolster electrochemical performance by increasing the contact area between the electrode and electrolyte, as well as reducing the diffusion path of Zn^{2+}. Functioning as a cathode material for ZIBs, it showcases a high capacity of 460 mA h g^{-1} at 0.1 A g^{-1}, outstanding rate capability, and impressive long-term cycling stability, retaining a specific capacity of 175 mA h g^{-1} at 4 A g^{-1} over 1500 cycles. The integration of CQDs and the formation of V^{4+} ions lead to an expanded interplanar spacing in V_2O_5, alongside enhanced electrical conductivity, thereby facilitating rapid charge transfer and ion diffusion.

Among the different V-based materials, tunnel-type VO_2(B) is considered an attractive host for AZIBs due to its suitable open structure capable of accommodating Zn^{2+} ions,[154] exhibiting a high specific capacity of 365 mA h g^{-1} at 0.05 A g^{-1} (equivalent to ~0.57 mol Zn^{2+} per VO_2).[155] However, the advancement of the high-performance VO_2(B) cathode is still hindered by slow electron and ion transport kinetics. Wu *et al.*[156] employed CA as the carbon source and obtained carbon quantum dots (CQDs) with an average size of 4 nm using a facile and scalable pyrolysis method. HRTEM images revealed well-dispersed carbon dots with a lattice spacing of 0.213 nm corresponding to the (100) lattice plane of CQDs. The VO_2/CQDs composite material was synthesized through a one-step hydrothermal reaction by combining a CQD aqueous solution with the $V_2O_5/H_2C_2O_4$ precursor. Importantly, the electrostatic interactions between the negatively charged carbon quantum dots (−7.7 mV) and the positively charged V_2O_5 (+10.3 mV) facilitated the uniform distribution of CQDs on vanadium oxide. The incorporation of

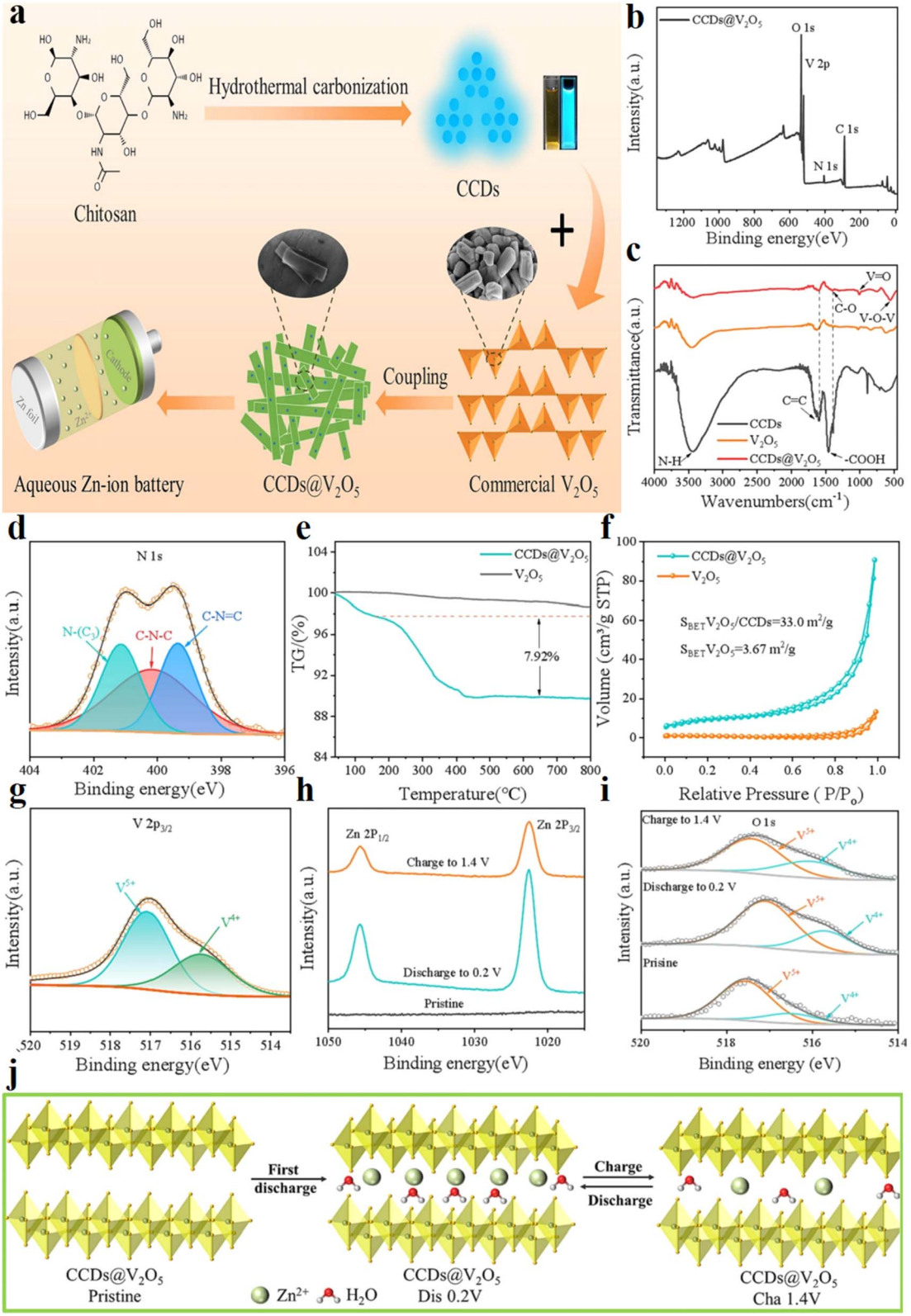

Fig. 13 Chitosan-derived CDs integrated with V_2O_5 nanobelts for aqueous zinc-ion batteries: (a) schematic of the synthesis of CCDs@V_2O_5 nanobelts; (b) XPS spectra of CCDs@V_2O_5; (c) infrared spectra of CCDs@V_2O_5, V_2O_5 and CCDs; (d) XPS spectrogram of N of CCDs@V_2O_5; (e) the TGA curves; (f) N_2 adsorption/desorption isotherms; (g) XPS spectrogram of V of CCDs@V_2O_5; (h and i) *ex situ* XPS spectra of V 2p and Zn 2p in different charge/discharge states at 0.1 A g^{-1}; (j) Zn^{2+} storage mechanism diagram of the CCDs@V_2O_5 electrode. Reproduced with permission.[152] Copyright 2024, Elsevier.

CQDs in the decoration process significantly enhances various aspects of the sample, including its surface area, presence of oxygen-containing functional groups, electrolyte wettability, reduction in charge-transfer resistance, and increase of ion diffusion coefficients. Consequently, the resulting VO_2/CQDs composite material demonstrates remarkable electrochemical performance metrics compared to the unmodified sample. These include a greater achievable capacity (427 mA h g^{-1} *versus* 373 mA h g^{-1}), increased specific energy (333 W h kg^{-1} compared to 287 W h kg^{-1}), and enhanced rate capability (72% retention *versus* 50% as the current density escalates from 0.2 to 8 A g^{-1}). Notably, the VO_2/CQDs cathode exhibits exceptional structural stability, allowing for consistent cycling performance over more than 2000 cycles. These results underscore the effectiveness of the CQD decoration strategy in improving electron/ion transport kinetics within cathode materials, thereby offering promising prospects for high-performance AZIBs.

5.4 Other kinds of batteries

5.4.1 Potassium ion batteries. Potassium-ion batteries (PIBs) share many similarities with SIBs.[157] Both are considered as supplements to LIBs due to the abundance of their resources. Their operating mechanisms are also relatively similar, and they are both incompatible with current mainstream lithium-ion graphite electrodes due to issues related to the ion radius. Specifically, this is because the ionic radius of potassium ions and sodium ions is much larger than that of lithium ions, resulting in the materials undergoing larger strain. During charging and discharging processes, this can lead to issues such as electrode material volume expansion and decreased reversibility. Therefore, there is an urgent need to develop suitable electrode materials.[158] Amorphous carbon emerges as an optimal option for fabricating high-performance PIBs and SIBs owing to its ample interlayer distance and elevated defect density. Nano-hollow carbon, a novel three-dimensional carbon nanomaterial, boasts features such as a high specific surface area, a variety of pore sizes, accessible inner cavities, and facile doping capabilities.[159] The hollow configuration of nano-hollow carbon enhances large-scale ion transport by minimizing diffusion distances and also helps reduce the negative volumetric expansion of anode materials during charge/discharge cycles.[160] However, precise control over the size of hollow carbon spheres significantly impacts the material's electrochemical performance. The silica-assisted template method for synthesizing hollow carbon spheres typically involves coating carbon materials onto silica templates of suitable sizes, followed by etching away the silica templates to yield hollow carbon spheres. Consequently, size-controlled hollow carbon spheres can be obtained by fine-tuning the size of the silica templates. Luo *et al.*[161] employed citrus peel as a carbon source to synthesize nitrogen-doped CDs through a 6-hour hydrothermal process at 180 °C, yielding CDs with a particle size of approximately 10 nm. The narrow particle size distribution of the CDs was confirmed using Gel Permeation Chromatography (GPC). Analysis *via* XRD, XPS, and FT-IR revealed the amorphous carbon phase of the CDs, along with abundant nitrogen and oxygen functional groups on their surfaces. The CDs possess a controllable surface structure, making them amenable to functionalization through both covalent and non-covalent bonds, thereby serving as effective connectors and inducers for constructing nanostructures with diverse morphologies. CDs obtained from citrus peel were utilized as modifiers to regulate the size of template SiO_2, facilitating the preparation of hollow carbon spheres with varying diameters. Throughout the synthesis of SiO_2 templates, the numerous surface functional groups of the CDs strongly interacted with the functional groups (such as hydroxyl groups) present in silicic acid and tetraethyl orthosilicate, thereby impeding the growth of SiO_2 spheres. By adjusting the quantity of added CDs, a series of hollow carbon spheres with diverse pore sizes were synthesized. Among these, nano-hollow carbon (HNC-60) anodes with a size of 50 nm, where '60' denotes the related number corresponding to the amount of carbon dots added, exhibited superior electrochemical performance for potassium/sodium storage. The remarkable performance of HNC-60 is attributed to its optimal size and hollow architecture, which reduce the ion diffusion distance and mitigate volumetric expansion during charge and discharge cycles. The pore structures of the carbon material were examined using the N_2 adsorption–desorption test. HNC-60 has a specific surface area of 733.3 m^2 g^{-1} and displays typical type IV isotherms, suggesting a hierarchical structure consisting of micropores and mesopores, potentially resulting from the internal pyrolysis of CDs. As an anode material for PIBs, HNC-60 retained a capacity of 252.3 mA h g^{-1} at 0.1 A g^{-1} after 200 cycles. Even after 1000 cycles, its reversible capacity was still 194.2 mA h g^{-1} (at 1 A g^{-1}). Similarly, in SIBs, HNC-60 demonstrated a reversible capacity of 269.2 mA h g^{-1} (150 cycles at 0.1 A g^{-1}). Remarkably, even at 1 A g^{-1}, the reversible capacity remained stable at 227.1 mA h g^{-1} after 1000 cycles. Lu *et al.*[162] combined glucose as the carbon source with Graphene Oxide (GO). They employed a two-step process involving microwave-assisted treatment and high-temperature annealing in a mixed Ar/H_2 atmosphere to introduce glucose carbon dots onto the surface of reduced graphene oxide (rGO), thus creating a high-performance anode (CDs@rGO) for PIBs. The CDs@rGO paper, possessing a 3D structure, facilitates improved kinetics by effectively reducing the electron and ion conduction distances. Additionally, the incorporation of CDs featuring O-containing functional groups promotes the orderly induction of K ions, facilitating the formation of a SEI on the electrode surface and preserving the integrity of the electrode structure. Furthermore, CDs can serve as a binder, ensuring the stability of the electrode structure while minimizing the impact of the binder on battery performance. As a result, the battery demonstrates a measured specific capacity of 310 mA h g^{-1} at 0.1 A g^{-1} with an ICE of about 44%. After 840 cycles at 0.2 A g^{-1}, a capacity of 244 mA h g^{-1} with an average decay rate of 0.03% per cycle is achieved. Furthermore, the CDs@rGO paper exhibits superior rate performance compared to other carbon-based PIB anodes, maintaining a capacity of 185 mA h g^{-1} at a current density of

500 mA g^{-1} after undergoing 6 consecutive current changes from 100 to 500 mA g^{-1}.

5.4.2 Metal–air batteries. The flexible metal–air battery has attracted widespread research and attention due to its remarkable theoretical energy density of 8100 W h kg^{-1},[163] as well as its environmentally friendly nature and highly compatible assembly with the existing electronic devices.[164] In metal–air batteries, the performance of the discharge process predominantly hinges on the efficiency of the oxygen reduction reaction (ORR) at the cathode electrode.[165] However, the practical application of commercial ORR catalysts for cathodes, such as Pt/C catalysts is limited in their further development due to factors such as exorbitant costs and inadequate stability, impeding their further advancement.[166]

Metal-free carbon materials have been extensively researched as non-precious metal catalysts for the oxygen reduction reaction.[167] Lai *et al.*[163] utilized phytic acid as both a carbon and phosphorus source to hydrothermally prepare the precursor of ORR catalysts in conjunction with graphene oxide (GO) nanosheets. During the hydrothermal process, the formation and simultaneous *in situ* decoration of phosphorus-doped carbon dots on the surface of GO takes place. Subsequently, the resulting sample undergoes further annealing at elevated temperatures to yield the final product, P-CD/G nanocomposites. XPS testing indicates that samples annealed at 900 °C have a phosphorus content of 2.31 at%. The introduction of P-doped carbon dots provides additional active sites, presenting an improved thermodynamic driving force. The P-CD/G nanocomposites demonstrate outstanding ORR performance, rivaling that of commercial Pt/C catalysts. When utilized as a cathode in an Al–air battery, this device demonstrates a remarkable power density of 157.3 mW cm^{-2}, surpassing the 151.5 mW cm^{-2} of a similar Pt/C battery.

Yang *et al.*[148] utilized sodium citrate as a carbon source, subjecting it to a two-hour calcination at 500 °C in a nitrogen atmosphere, followed by washing to eliminate sodium salts and impurities, and obtained carbon dots. These CDs, rich in oxygen-containing functional groups, competed with 2-methylimidazole for coordination with Co^{2+}. Moreover, during assembly, small-sized carbon dots became integrated into the framework structure of zeolitic imidazolate frameworks (ZIF-67). Subsequent pyrolysis transformed the organic ligand and carbon dots within ZIF-67(CDs) into N-doped porous polyhedral carbon CoCN (CDs). Subsequently, platinum was anchored onto the CoCN (CDs) to yield bimetallic catalysts termed PtCoCN (CDs), characterized by a low platinum loading (<5 wt%) (Fig. 12b). HRTEM images reveal that carbon dots with a lattice spacing of 0.25 nm are well dispersed and assembled within the catalyst. XRD and Raman spectroscopy confirm that the introduction of carbon dots enhances the graphitization degree of the material and the crystallinity of Co, thereby facilitating rapid electron transfer. Additionally, the abundant oxygen-containing functional groups on the CDs can coordinate with Co atoms *via* Co–O bonds, providing new catalytic active sites. The incorporation of carbon dots enhances the interaction between Pt and CoCN (CD), resulting in a decrease in the d-band center of Pt, weakening the adsorption of intermediates, accelerating the kinetics of the ORR, and enhancing catalytic stability. As a result, PtCoCN (CDs) with optimized levels of carbon dots exhibit commendable catalytic performance towards the ORR in an alkaline medium. Furthermore, when employed as the cathode catalyst in an assembled zinc–air battery (ZAB), PtCoCN (CDs) demonstrates a high peak power density of 194.2 mW cm^{-2} and satisfactory stability. Notably, the voltage efficiency only decreases by 7.7% after 100 hours of charge and discharge.

6. Conclusions and outlook

The distinctive attributes of BCDs, including their easy dispersibility, adjustable size, low toxicity, biocompatibility, and customizable surface functional groups, pave the way for extensive and impactful applications. Their low-cost, straightforward synthesis routes and environmental benefits further accentuate their unique competitive edge among various functional carbon materials. The carbon source of BCDs originates from sustainable biological derivatives, a key feature that differentiates them from traditional chemical carbon dots. This distinction fundamentally influences both their synthesis and application characteristics.

From a synthetic standpoint, selecting the appropriate carbon source is paramount. When using organisms directly as carbon sources for synthesis, despite the advantages of simple preprocessing and low cost, the complexity and instability of organism-derived components pose challenges in preparing functional materials. The intricate nature of reaction substrates and unclear reaction mechanisms make designing and controlling the structure of functional materials difficult, resulting in inefficient development in this field due to ineffective prediction and screening of experimental conditions. Although the richness of biomass as a raw material partially compensates for the low content of active components in organisms, it inevitably leads to low material utilization and high energy consumption during the production process. Therefore, a potential future research direction involves exploring reliable reaction mechanisms to guide synthesis experiments, including material selection, process optimization, and product modification. Additionally, further purification or modification and functionalization studies of the products are crucial. The abundant nitrogen, phosphorus, sulfur, and other element contents in biomass enable self-doping possibilities during the synthesis process. Carbon dots derived from organisms may acquire nitrogen, phosphorus, and sulfur-containing surface functional groups without further treatment, providing them with richer surface chemical properties. This approach currently dominates research for the synthesis and modification of BCDs. Furthermore, synthesis strategies for chemical carbon dots also serve as references for biomass carbon dot synthesis. For example, the use of exogenous doping agents is a widely applied and effective method for modifying biomass carbon dot materials. Even small amounts of chemical doping agents can significantly enhance material performance without undermining the original intention of creating green and environmentally friendly BCDs. In future

research, combining practical application scenarios and demands with effective methods from chemical carbon dot synthesis may yield unexpected results. For instance, in biomedical applications, cautious consideration is necessary when introducing substances with biological toxicity, while carbon dots used in energy storage applications can circumvent this limitation.

Currently, the most prevalent biomass carbon sources in use are certain single-component, highly reactive biomass derivatives such as CA, glucose, and amino acids. Despite the increased costs associated with using high-purity reagents and the environmental concerns they may raise, they still offer distinct advantages compared to raw materials used in traditional chemical synthesis of carbon dots. The advantage of using such raw materials as carbon sources compared to organisms lies in eliminating the unstable factors of biological raw materials, simplifying the post-processing of products, and facilitating effective exploration of the mechanisms during the reaction process. Moreover, the implementation of environmentally friendly production processes for raw materials, and the industrialization of complete production processes, are also vital considerations for the application of such biomass carbon sources.

In this comprehensive review, the primary focus is on the intricate relationship between the application strategies of BCDs in energy storage batteries and their structural attributes. A detailed exploration of this structure–function correlation is instrumental in inspiring innovative approaches for the design and utilization of BCDs. Within the realm of battery materials, the small size of BCDs facilitates easy dispersion, while their graphitic carbon core enhances electron transfer capabilities, rendering them highly advantageous in various electrochemical applications such as electrocatalysis and energy storage batteries. Carbon dots can function as versatile frameworks for loading active materials, boasting adjustable sizes as an added advantage. Their abundant surface functional groups directly influence interactions at phase interfaces. For instance, they can serve as electrolyte additives, regulating the growth of metal dendrites at the electrolyte–electrode interface. Additionally, they serve as precursors for synthesizing functional materials, exerting influence on physicochemical changes during material formation through their surface chemical properties. For instance, carbon dots containing hydroxyl and carboxyl groups can bind to silicates *via* hydrogen bonding in aqueous solutions, thus constraining the growth of silica template particles and indirectly governing the porosity and morphology of electrode materials. Alternatively, carbon dots themselves can be dispersed and embedded into precursor materials, undergoing further physicochemical transformations to yield novel functional materials. The versatile properties of BCDs render their application areas flexible and extensive, with considerable potential for expansion, offering abundant avenues for exploration. It is noteworthy that their application in different fields can blend with each other. For example, simultaneously utilizing their electrochemical properties and optical characteristics can lead to the development of fluorescent wearable battery devices, and exploration in interdisciplinary fields may generate more creative strategies.

Data availability

All the data supporting this article have been included in the main text.

Author contributions

Dongyang Cai: writing – review & editing, writing – original draft, investigation, data curation, conceptualization. Xue Zhong: formal analysis, data curation. Laiqiang Xu: writing – review & editing, supervision, funding acquisition. Yu Xiong: writing – review & editing, supervision. Wentao Deng: methodology, formal analysis. Guoqiang Zou: writing – review & editing, supervision, conceptualization. Hongshuai Hou: writing – review & editing, supervision, funding acquisition. Xiaobo Ji: writing – review & editing, supervision, conceptualization.

Conflicts of interest

There are no conflicts to declare.

Acknowledgements

This work was financially supported by the National Natural Science Foundation of China (52074359, 22379165, U21A20284, and U22B2069), the Science and Technology Innovation Program of Hunan Province (2021RC3014), the Hunan Provincial Science and Technology Plan (2024JJ6709), the Changsha Natural Science Foundation (kq2402248), the Open Research Fund of Science and Technology Innovation Platform of Key Laboratory of Renewable Energy Electric-Technology of Hunan Province (2024ZNDL006), and Changsha University of Science & Technology.

References

1 V. Georgakilas, J. A. Perman, J. Tucek and R. Zboril, Broad family of carbon nanoallotropes: Classification, chemistry, and applications of fullerenes, carbon dots, nanotubes, graphene, nanodiamonds, and combined superstructures, *Chem. Rev.*, 2015, **115**(11), 4744–4822.
2 X. Y. Xu, R. Ray, Y. L. Gu, H. J. Ploehn, L. Gearheart, K. Raker and W. A. Scrivens, Electrophoretic analysis and purification of fluorescent single-walled carbon nanotube fragments, *J. Am. Chem. Soc.*, 2004, **126**(40), 12736–12737.
3 M. L. Liu, B. B. Chen, C. M. Li and C. Z. Huang, Carbon dots: synthesis, formation mechanism, fluorescence origin and sensing applications, *Green Chem.*, 2019, **21**(3), 449–471.
4 R. Q. Cheng, Y. E. Xiang, R. T. Guo, L. Li, G. Q. Zou, C. P. Fu, H. S. Hou and X. B. Ji, Structure and interface modification of carbon dots for electrochemical energy application, *Small*, 2021, **17**(40), 2102091.

5 F. Liu, S. H. Xu, W. B. Gong, K. T. Zhao, Z. M. Wang, J. Luo, C. S. Li, Y. Sun, P. Xue, C. L. Wang, L. Wei, Q. W. Li and Q. C. Zhang, Fluorescent fiber-shaped aqueous zinc-ion batteries for bifunctional multicolor-emission/energy-storage textiles, *ACS Nano*, 2023, **17**(18), 18494–18506.
6 Y. X. Jiang, T. S. Zhao, W. J. Xu and Z. L. Peng, Red/NIR C-dots: A perspective from carbon precursors, photoluminescence tuning and bioapplications, *Carbon*, 2024, **219**, 118838.
7 R. T. Guo, L. Li, B. W. Wang, Y. G. Xiang, G. Q. Zou, Y. R. Zhu, H. S. Hou and X. B. Ji, Functionalized carbon dots for advanced batteries, *Energy Storage Mater.*, 2021, **37**, 8–39.
8 J. H. Shen, Y. H. Zhu, X. L. Yang and C. Z. Li, Graphene quantum dots: emergent nanolights for bioimaging, sensors, catalysis and photovoltaic devices, *Chem. Commun.*, 2012, **48**(31), 3686–3699.
9 R. Simoes, J. Rodrigues, V. Neto, T. Monteiro and G. Gonçalves, Carbon dots: A bright future as anticounterfeiting encoding agents, *Small*, 2024, **20**(28), 2311526.
10 A. Cayuela, M. L. Soriano, C. Carrillo-Carrión and M. Valcárcel, Semiconductor and carbon-based fluorescent nanodots: the need for consistency, *Chem. Commun.*, 2016, **52**(7), 1311–1326.
11 T. C. Wareing, P. Gentile and A. N. Phan, Biomass-based carbon dots: Current development and future perspectives, *ACS Nano*, 2021, **15**(10), 15471–15501.
12 F. J. Chao-Mujica, L. Garcia-Hernández, S. Camacho-López, M. Camacho-López, M. A. Camacho-López, D. R. Contreras, A. Pérez-Rodríguez, J. P. Peña-Caravaca, A. Páez-Rodríguez, J. G. Darias-Gonzalez, L. Hernandez-Tabares, O. Arias de Fuentes, E. Prokhorov, N. Torres-Figueredo, E. Reguera and L. F. Desdin-García, Carbon quantum dots by submerged arc discharge in water: Synthesis, characterization, and mechanism of formation, *J. Appl. Phys.*, 2021, **129**, 163301.
13 A. Ananthanarayanan, X. W. Wang, P. Routh, B. Sana, S. Lim, D. H. Kim, K. H. Lim, J. Li and P. Chen, Facile synthesis of graphene quantum dots from 3D graphene and their application for Fe^{3+} sensing, *Adv. Funct. Mater.*, 2014, **24**(20), 3021–3026.
14 J. G. Zhou, C. Booker, R. Y. Li, X. T. Zhou, T. K. Sham, X. L. Sun and Z. F. Ding, An electrochemical avenue to blue luminescent nanocrystals from multiwalled carbon nanotubes (MWCNTs), *J. Am. Chem. Soc.*, 2007, **129**(4), 744–745.
15 C. K. Chua, Z. Sofer, P. Simek, O. Jankovsky, K. Klímová, S. Bakardjieva, S. H. Kucková and M. Pumera, Synthesis of strongly fluorescent graphene quantum dots by cage-opening Buckminsterfullerene, *ACS Nano*, 2015, **9**(3), 2548–2555.
16 T. K. Nideep, M. Ramya, V. P. N. Nampoori and M. Kailasnath, Optical limiting and optical properties of water soluble CdTe quantum dots prepared through a colloidal chemical route, *Optik*, 2019, **179**, 1101–1108.
17 Q. J. Lu, J. H. Deng, Y. X. Hou, H. Y. Wang, H. T. Li, Y. Y. Zhang and S. Z. Yao, Hydroxyl-rich C-dots synthesized by a one-pot method and their application in the preparation of noble metal nanoparticles, *Chem. Commun.*, 2015, **51**(33), 7164–7167.
18 S. Dey, A. Govindaraj, K. Biswas and C. N. R. Rao, Luminescence properties of boron and nitrogen doped graphene quantum dots prepared from arc-discharge-generated doped graphene samples, *Chem. Phys. Lett.*, 2014, **595**, 203–208.
19 Z. A. Qiao, Y. F. Wang, Y. Gao, H. W. Li, T. Y. Dai, Y. L. Liu and Q. S. Huo, Commercially activated carbon as the source for producing multicolor photoluminescent carbon dots by chemical oxidation, *Chem. Commun.*, 2010, **46**(46), 8812–8814.
20 X. T. Zheng, A. Ananthanarayanan, K. Q. Luo and P. Chen, Glowing graphene quantum dots and carbon dots: Properties, syntheses, and biological applications, *Small*, 2015, **11**(14), 1620–1636.
21 Y. L. Xu, C. Wang, T. Jiang, G. X. Ran and Q. J. Song, Cadmium induced aggregation of orange-red emissive carbon dots with enhanced fluorescence for intracellular imaging, *J. Hazard. Mater.*, 2022, **427**, 128092.
22 B. A. Yuan, Z. Xie, P. Chen and S. Y. Zhou, Highly efficient carbon dots and their nanohybrids for trichromatic white LEDs, *J. Mater. Chem. C*, 2018, **6**(22), 5957–5963.
23 Y. L. Xu, C. Wang, H. Zhuo, D. R. Zhou and Q. J. Song, The function-oriented precursor selection for the preparation of carbon dots, *Nano Res.*, 2023, **16**(8), 11221–11249.
24 A. Abbas, L. T. Mariana and A. N. Phan, Biomass-waste derived graphene quantum dots and their applications, *Carbon*, 2018, **140**, 77–99.
25 R. S. Li, P. F. Gao, H. Z. Zhang, L. L. Zheng, C. M. Li, J. Wang, Y. F. Li, F. Liu, N. Li and C. Z. Huang, Chiral nanoprobes for targeting and long-term imaging of the Golgi apparatus, *Chem. Sci.*, 2017, **8**(10), 6829–6835.
26 J. Liu, T. Y. Kong and H. M. Xiong, Mulberry-leaves-derived red-emissive carbon dots for feeding silkworms to produce brightly fluorescent silk, *Adv. Mater.*, 2022, **34**(16), 2200152.
27 W. X. Meng, X. Bai, B. Y. Wang, Z. Y. Liu, S. Y. Lu and B. Yang, Biomass-derived carbon dots and their applications, *Energy Environ. Mater.*, 2019, **2**(3), 172–192.
28 J. Gan, L. Z. Chen, Z. J. Chen, J. L. Zhang, W. J. Yu, C. X. Huang, Y. Wu and K. Zhang, Lignocellulosic biomass-based carbon dots: Synthesis processes, properties, and applications, *Small*, 2023, **19**(48), 2304066.
29 T. R. Kuang, M. Y. Jin, X. R. Lu, T. Liu, H. Vahabi, Z. P. Gu and X. Gong, Functional carbon dots derived from biomass and plastic wastes, *Green Chem.*, 2023, **25**(17), 6581–6602.
30 M. Y. Fang, B. Y. Wang, X. L. Qu, S. R. Li, J. S. Huang, J. N. Li, S. Y. Lu and N. Zhou, State-of-the-art of biomass-derived carbon dots: Preparation, properties, and applications, *Chin. Chem. Lett.*, 2024, **35**(1), 108423.
31 S. Mathew and B. Mathew, A review on the synthesis, properties, and applications of biomass derived carbon dots, *Inorg. Chem. Commun.*, 2023, **156**, 111223.

32 H. E. Emam, Carbon quantum dots derived from polysaccharides: Chemistry and potential applications, *Carbohydr. Polym.*, 2024, **324**, 121503.
33 H. C. Liu, J. Ding, K. Zhang and L. Ding, Construction of biomass carbon dots based fluorescence sensors and their applications in chemical and biological analysis, *TrAC, Trends Anal. Chem.*, 2019, **118**, 315–337.
34 J. Y. Wu, T. Y. Chen, S. B. Ge, W. Fan, H. Wang, Z. F. Zhang, E. Lichtfouse, T. Van Tran, R. K. Liew, M. Rezakazemi and R. Z. Huang, Synthesis and applications of carbon quantum dots derived from biomass waste: a review, *Environ. Chem. Lett.*, 2023, **21**(6), 3393–3424.
35 Y. Lou, X. Y. Hao, L. Liao, K. Y. Zhang, S. P. Chen, Z. Y. Li, J. Ou, A. M. Qin and Z. Li, Recent advances of biomass carbon dots on syntheses, characterization, luminescence mechanism, and sensing applications, *Nano Sel.*, 2021, **2**(6), 1117–1145.
36 W. J. Cao, W. J. Zhang, L. Dong, Z. Ma, J. S. Xu, X. L. Gu and Z. P. Chen, Progress on quantum dot photocatalysts for biomass valorization, *Exploration*, 2023, **3**, 20220169.
37 J. S. Wei, C. Ding, P. Zhang, H. Ding, X. Q. Niu, Y. Y. Ma, C. Li, Y. G. Wang and H. M. Xiong, Robust negative electrode materials derived from carbon dots and porous hydrogels for high-performance hybrid supercapacitors, *Adv. Mater.*, 2019, **31**, 1806197.
38 H. X. Liu, L. Q. Xu, H. Y. Tu, Z. Luo, F. J. Zhu, W. T. Deng, G. Q. Zou, H. S. Hou and X. B. Ji, Interfacial interaction of multifunctional GQDs reinforcing polymer electrolytes for all-solid-state Li battery, *Small*, 2023, **19**, 2301275.
39 G. Y. Zhang, X. Liu, L. Wang and H. G. Fu, Recent advances of biomass derived carbon-based materials for efficient electrochemical energy devices, *J. Mater. Chem. A*, 2022, **10**(17), 9277–9307.
40 M. T. Genc, G. Yanalak, G. Arslan and I. H. Patir, Green preparation of carbon quantum dots using gingko biloba to sensitize TiO_2 for the photohydrogen production, *Mater. Sci. Semicond. Process.*, 2020, **109**, 104945.
41 M. J. Krysmann, A. Kelarakis and E. P. Giannelis, Photoluminescent carbogenic nanoparticles directly derived from crude biomass, *Green Chem.*, 2012, **14**(11), 3141–3145.
42 W. B. Lu, X. Y. Qin, S. Liu, G. H. Chang, Y. W. Zhang, Y. L. Luo, A. M. Asiri, A. O. Al-Youbi and X. P. Sun, Economical, green synthesis of fluorescent carbon nanoparticles and their use as probes for sensitive and selective detection of mercury(II) ions, *Anal. Chem.*, 2012, **84**(12), 5351–5357.
43 X. Gao, X. D. Ji, T. T. Nguyen, X. C. Gong, R. S. Chai and M. H. Guo, A novel composite material with wood-based carbon quantum dots modified Bi_2MoO_6 hollow microspheres, *Vacuum*, 2019, **164**, 256–264.
44 Y. Qian, Y. Z. Liang, W. Q. Zhang, B. J. Xi and N. Lin, Thermal polymerization of ion-modified carbon dots into multi-functional LiF-carbon interface for stabilizing SiO anode, *Energy Storage Mater.*, 2023, **63**, 102996.
45 M. Q. He, J. Zhang, H. Wang, Y. R. Kong, Y. M. Xiao and W. Xu, Material and optical properties of fluorescent carbon quantum dots fabricated from lemon juice *via* hydrothermal reaction, *Nanoscale Res. Lett.*, 2018, **13**, 175.
46 M. Thakur, A. Mewada, S. Pandey, M. Bhori, K. Singh, M. Sharon and M. Sharon, Milk-derived multi-fluorescent graphene quantum dot-based cancer theranostic system, *Mater. Sci. Eng., C*, 2016, **67**, 468–477.
47 Q. Wang, X. Liu, L. C. Zhang and Y. Lv, Microwave-assisted synthesis of carbon nanodots through an eggshell membrane and their fluorescent application, *Analyst*, 2012, **137**(22), 5392–5397.
48 L. H. Shi, B. Zhao, X. F. Li, G. M. Zhang, Y. Zhang, C. Dong and S. M. Shuang, Eco-friendly synthesis of nitrogen-doped carbon nanodots from wool for multicolor cell imaging, patterning, and biosensing, *Sensor. Actuator. B Chem.*, 2016, **235**, 316–324.
49 C. D. D. S. Barbosa, J. R. Corrêa, G. A. Medeiros, G. Barreto, K. G. Magalhaes, A. L. de Oliveira, J. Spencer, M. O. Rodrigues and B. A. D. Neto, Carbon dots (C-dots) from cow manure with impressive subcellular selectivity tuned by simple chemical modification, *Chem.–Eur. J.*, 2015, **21**(13), 5055–5060.
50 Y. M. Wang, J. Sun, B. He and M. Feng, Synthesis and modification of biomass derived carbon dots in ionic liquids and their application: A mini review, *Green Chem. Eng.*, 2020, **1**(2), 94–108.
51 B. Qin, M. Wang, S. Wu, Y. Li, C. Liu, Y. Zhang and H. Fan, Carbon dots confined nanosheets assembled $NiCo_2S_4$@CDs cross-stacked architecture for enhanced sodium ion storage, *Chin. Chem. Lett.*, 2023, **35**, 108921.
52 R. Q. Cheng, M. Jiang, K. Q. Li, M. L. Guo, J. Zhang, J. M. Ren, P. Y. Meng, R. H. Li and C. P. Fu, Dimensional engineering of carbon dots derived sulfur and nitrogen co-doped carbon as efficient oxygen reduction reaction electrocatalysts for aluminum-air batteries, *Chem. Eng. J.*, 2021, **425**, 130603.
53 H. Zhang, J. He, Y. Y. Xiong, H. X. Mu, Y. Q. Deng and Q. Zhao, Antibacterial mechanism analysis and structural design of amino acid-based carbon dots, *J. Mater. Sci.*, 2023, **58**(11), 4954–4969.
54 Z. Y. Yan, Z. W. Zhang and J. Q. Chen, Biomass-based carbon dots: Synthesis and application in imatinib determination, *Sensor. Actuator. B Chem.*, 2016, **225**, 469–473.
55 Y. Wang, Q. Wang, W. X. Liu, Y. L. Wei, S. S. Wang, S. H. Luo, Y. H. Zhang, P. Q. Hou, S. X. Yan, X. Liu and J. Guo, Hydrangea-like MoS_2/carbon dots anode for high-performance sodium storage, *J. Colloid Interface Sci.*, 2024, **655**, 407–416.
56 X. Liu, T. Z. Li, Y. Hou, Q. H. Wu, J. Yi and G. L. Zhang, Microwave synthesis of carbon dots with multi-response using denatured proteins as carbon source, *RSC Adv.*, 2016, **6**(14), 11711–11718.
57 D. S. Achilleos, H. Kasap and E. Reisner, Photocatalytic hydrogen generation coupled to pollutant utilisation using carbon dots produced from biomass, *Green Chem.*, 2020, **22**(9), 2831–2839.

58 W. D. Li, Y. Liu, M. Wu, X. L. Feng, S. A. T. Redfern, Y. Shang, X. Yong, T. Feng, K. F. Wu, Z. Y. Liu, B. J. Li, Z. M. Chen, J. S. Tse, S. Y. Lu and B. Yang, Carbon-quantum-dots-loaded ruthenium nanoparticles as an efficient electrocatalyst for hydrogen production in alkaline media, *Adv. Mater.*, 2018, **30**(31), 1800676.

59 S. Tang, Y. F. Liu, H. Opoku, M. Gregorsson, P. J. Zhang, E. Auroux, D. F. Dang, A. V. Mudring, T. Wågberg, L. Edman and J. Wang, Fluorescent carbon dots from birch leaves for sustainable electroluminescent devices, *Green Chem.*, 2023, **25**(23), 9884–9895.

60 H. Ashraf and B. D. Karahan, Biowaste valorization into valuable nanomaterials: Synthesis of green carbon nanodots and anode material for lithium-ion batteries from watermelon seeds, *Mater. Res. Bull.*, 2024, **169**, 112492.

61 D. S. Achilleos, W. X. Yang, H. Kasap, A. Savateev, Y. Markushyna, J. R. Durrant and E. Reisner, Solar reforming of biomass with homogeneous carbon dots, *Angew. Chem. Int. Ed.*, 2020, **59**(41), 18184–18188.

62 H. Vanessa, W. S. Wang, D. Cornelia, W. Simon, T. Martin and P. Wolfgang, Microwave-assisted one-step synthesis of white light-emitting carbon dot suspensions, *Opt. Mater.*, 2018, **80**, 110–119.

63 C. X. Yang, R. Ogaki, L. Hansen, J. Kjems and B. M. Teo, Theranostic carbon dots derived from garlic with efficient anti-oxidative effects towards macrophages, *RSC Adv.*, 2015, **5**(118), 97836–97840.

64 X. Y. Qin, W. B. Lu, A. M. Asiri, A. O. Al-Youbi and X. P. Sun, Microwave-assisted rapid green synthesis of photoluminescent carbon nanodots from flour and their applications for sensitive and selective detection of mercury(II) ions, *Sensor. Actuator. B Chem.*, 2013, **184**, 156–162.

65 Y. J. Feng, D. Zhong, H. Miao and X. M. Yang, Carbon dots derived from rose flowers for tetracycline sensing, *Talanta*, 2015, **140**, 128–133.

66 A. Suryawanshi, M. Biswal, D. Mhamane, R. Gokhale, S. Patil, D. Guin and S. Ogale, Large scale synthesis of graphene quantum dots (GQDs) from waste biomass and their use as an efficient and selective photoluminescence on-off-on probe for Ag^{+} ions, *Nanoscale*, 2014, **6**(20), 11664–11670.

67 M. M. Titirici, M. Antonietti and N. Baccile, Hydrothermal carbon from biomass: a comparison of the local structure from poly- to monosaccharides and pentoses/hexoses, *Green Chem.*, 2008, **10**(11), 1204–1212.

68 B. De and N. Karak, A green and facile approach for the synthesis of water soluble fluorescent carbon dots from banana juice, *RSC Adv.*, 2013, **3**(22), 8286–8290.

69 W. R. Hu, W. H. Tong, Y. L. Li, Y. Xie, Y. D. Chen, Z. Q. Wen, S. F. Feng, X. Q. Wang, P. Y. Li, Y. B. Wang and Y. K. Zhang, Hydrothermal route-enabled synthesis of sludge-derived carbon with oxygen functional groups for bisphenol A degradation through activation of peroxymonosulfate, *J. Hazard. Mater.*, 2020, **388**, 121801.

70 X. Feng, Y. Q. Jiang, J. P. Zhao, M. Miao, S. M. Cao, J. H. Fang and L. Y. Shi, Easy synthesis of photoluminescent N-doped carbon dots from winter melon for bio-imaging, *RSC Adv.*, 2015, **5**(40), 31250–31254.

71 X. H. Wang, L. Xu, S. B. Ge, S. Y. Foong, R. K. Liew, W. W. F. Chong, M. Verma, M. Naushad, Y. K. Park, S. S. Lam, Q. Li and R. Z. Huang, Biomass-based carbon quantum dots for polycrystalline silicon solar cells with enhanced photovoltaic performance, *Energy*, 2023, **274**, 127354.

72 N. Papaioannou, M. M. Titirici and A. Sapelkin, Investigating the effect of reaction time on carbon dot formation, structure, and optical properties, *ACS Omega*, 2019, **4**(26), 21658–21665.

73 T. Pal, S. Mohiyuddin and G. Packirisamy, Facile and green synthesis of multicolor fluorescence carbon dots from curcumin: *In vitro* and *in vivo* bioimaging and other applications, *ACS Omega*, 2018, **3**(1), 831–843.

74 U. Abd Rani, L. Y. Ng, C. Y. Ng, E. Mahmoudi and N. H. H. Hairom, Photocatalytic degradation of crystal violet dye using sulphur-doped carbon quantum dots, *Mater. Today: Proc.*, 2021, **46**, 1934–1939.

75 H. Q. Song, Y. H. Li, L. Shang, Z. Y. Tang, T. R. Zhang and S. Y. Lu, Designed controllable nitrogen-doped carbon-dots-loaded MoP nanoparticles for boosting hydrogen evolution reaction in alkaline medium, *Nano Energy*, 2020, **72**, 104730.

76 D. Pooja, S. Saini, A. Thakur, B. Kumar, S. Tyagi and M. K. Nayak, A "Turn-On" thiol functionalized fluorescent carbon quantum dot based chemosensory system for arsenite detection, *J. Hazard. Mater.*, 2017, **328**, 117–126.

77 G. Wang, G. L. Guo, D. Chen, Z. D. Liu, X. H. Zheng, A. L. Xu, S. W. Yang and G. Q. Ding, Facile and highly effective synthesis of controllable lattice sulfur-doped graphene quantum dots *via* hydrothermal treatment of durian, *ACS Appl. Mater. Interfaces*, 2018, **10**(6), 5750–5759.

78 W. X. Wang, J. Chen, D. K. Wang, Y. M. Shen, L. K. Yang, T. Zhang and J. Ge, Facile synthesis of biomass waste-derived fluorescent N, S, P co-doped carbon dots for detection of Fe^{3+} ions in solutions and living cells, *Anal. Methods*, 2021, **13**(6), 789–795.

79 S. H. Miao, K. Liang, J. J. Zhu, B. Yang, D. Y. Zhao and B. Kong, Hetero-atom-doped carbon dots: Doping strategies, properties and applications, *Nano Today*, 2020, **33**, 100879.

80 Y. P. Zhang, L. L. Wang, H. Xu, J. M. Cao, D. Chen and W. Han, 3D chemical cross-linking structure of black phosphorus@CNTs hybrid as a promising anode material for lithium ion batteries, *Adv. Funct. Mater.*, 2020, **30**(12), 1909372.

81 Z. Y. Yuan, L. L. Wang, D. D. Li, J. M. Cao and W. Han, Carbon-reinforced Nb_2CT_x MXene/MoS_2 nanosheets as a superior rate and high-capacity anode for sodium-ion batteries, *ACS Nano*, 2021, **15**(4), 7439–7450.

82 Z. Jiao, R. M. Gao, H. H. Tao, S. A. Yuan, L. Q. Xu, S. S. Xia and H. J. Zhang, Intergrown SnO_2-TiO_2@graphene ternary composite as high-performance lithium-ion battery anodes, *J. Nanopart. Res.*, 2016, **18**, 307.

83 L. J. Li, Q. H. Chen, M. Z. Jiang, T. X. Ning, L. Tan, X. H. Zhang, J. C. Zheng, J. X. Wang, Q. Wu, X. B. Ji, F. X. Wu and K. Y. Zou, Uncovering mechanism behind tungsten bulk/grain-boundary modification of Ni-rich cathode, *Energy Storage Mater.*, 2025, **75**, 104016.

84 C. Z. Yuan, H. B. Wu, Y. Xie and X. W. Lou, Mixed transition-metal oxides: Design, synthesis, and energy-related applications, *Angew. Chem. Int. Ed.*, 2014, **53**(6), 1488–1504.

85 J. Sun, G. Y. Zheng, H. W. Lee, N. Liu, H. T. Wang, H. B. Yao, W. S. Yang and Y. Cui, Formation of stable phosphorus-carbon bond for enhanced performance in black phosphorus nanoparticle-graphite composite battery anodes, *Nano Lett.*, 2014, **14**(8), 4573–4580.

86 B. J. Chen, L. Chen, L. H. Zu, Y. T. Feng, Q. M. Su, C. Zhang and J. H. Yang, Zero-strain high-capacity silicon/carbon anode enabled by a MOF-derived space-confined single-atom catalytic strategy for lithium-ion batteries, *Adv. Mater.*, 2022, **34**(21), 2200894.

87 S. Y. Dong, N. Lv, Y. L. Wu, G. Y. Zhu and X. C. Dong, Lithium-ion and sodium-ion hybrid capacitors: from insertion-type materials design to devices construction, *Adv. Funct. Mater.*, 2021, **31**(21), 2100455.

88 Y. F. He, L. Wang, A. P. Wang, B. Zhang, H. Pham, J. Park and X. M. He, Insight into uniform filming of LiF-rich interphase *via* synergistic adsorption for high-performance lithium metal anode, *Exploration*, 2024, **4**, 20230114.

89 K. Y. Zou, M. Z. Jiang, T. X. Ning, L. Tan, J. C. Zheng, J. X. Wang, X. B. Ji and L. J. Li, Thermodynamics-directed bulk/grain-boundary engineering for superior electrochemical durability of Ni-rich cathode, *J. Energy Chem.*, 2024, **97**, 321–331.

90 Y. F. Tian, G. Li, D. X. Xu, Z. Y. Lu, M. Y. Yan, J. Wan, J. Y. Li, Q. Xu, S. Xin, R. Wen and Y. G. Guo, Micrometer-sized $SiMg_yO_x$ with stable internal structure evolution for high-performance Li-ion battery anodes, *Adv. Mater.*, 2022, **34**(15), 2200672.

91 Y. M. Sun, H. W. Lee, Z. W. Seh, N. Liu, J. Sun, Y. Z. Li and Y. Cui, High-capacity battery cathode prelithiation to offset initial lithium loss, *Nat. Energy*, 2016, **1**, 15008.

92 Z. X. Xiao, C. H. Yu, X. Q. Lin, X. Chen, C. X. Zhang, H. R. Jiang, R. F. Zhang and F. Wei, TiO_2 as a multifunction coating layer to enhance the electrochemical performance of SiO_x@TiO_2@C composite as anode material, *Nano Energy*, 2020, **77**, 105082.

93 M. Chhowalla, H. S. Shin, G. Eda, L. J. Li, K. P. Loh and H. Zhang, The chemistry of two-dimensional layered transition metal dichalcogenide nanosheets, *Nat. Chem.*, 2013, **5**(4), 263–275.

94 M. Ghidiu, M. R. Lukatskaya, M. Q. Zhao, Y. Gogotsi and M. W. Barsoum, Conductive two-dimensional titanium carbide 'clay' with high volumetric capacitance, *Nature*, 2014, **516**(7529), 78.

95 M. Lu, H. J. Li, W. J. Han, J. N. Chen, W. Shi, J. H. Wang, X. M. Meng, J. G. Qi, H. B. Li, B. S. Zhang, W. Zhang and W. T. Zheng, 2D titanium carbide (MXene) electrodes with lower-F surface for high performance lithium-ion batteries, *J. Energy Chem.*, 2019, **31**, 148–153.

96 L. Lu, G. Z. Guan, J. Wang, W. X. Meng, S. Q. Li, Y. J. Zhang and F. M. Guo, Nitrogen-doped carbon dots modified double transition metal MXene ($Ti_2NbC_2T_x$) for superior lithium/sodium-ion storage, *Chem. Eng. J.*, 2024, **480**, 147999.

97 H. Y. Pei, Q. Yang, J. K. Yu, H. Q. Song, S. Y. Zhao, G. I. N. Waterhouse, J. L. Guo and S. Y. Lu, Self-supporting carbon nanofibers with Ni-single-atoms and uniformly dispersed Ni-nanoparticles as scalable multifunctional hosts for high energy density lithium-sulfur batteries, *Small*, 2022, **18**(27), 2202037.

98 K. S. Huang, S. Bi, B. Kurt, C. Y. Xu, L. Y. Wu, Z. W. Li, G. Feng and X. G. Zhang, Regulation of SEI formation by anion receptors to achieve ultra-stable lithium-metal batteries, *Angew. Chem. Int. Ed.*, 2021, **60**(35), 19232–19240.

99 H. Chen, Y. F. Yang, D. T. Boyle, Y. K. Jeong, R. Xu, L. S. de Vasconcelos, Z. J. Huang, H. S. Wang, H. X. Wang, W. X. Huang, H. Q. Li, J. Y. Wang, H. K. Gu, R. Matsumoto, K. Motohashi, Y. Nakayama, K. J. Zhao and Y. Cui, Free-standing ultrathin lithium metal-graphene oxide host foils with controllable thickness for lithium batteries, *Nat. Energy*, 2021, **6**(8), 790–798.

100 H. Y. Tu, S. Li, Z. Luo, L. Q. Xu, H. Zhang, Y. E. Xiang, W. T. Deng, G. Q. Zou, H. S. Hou and X. B. Ji, Bi-doped carbon dots for a stable lithium metal anode, *Chem. Commun.*, 2022, **58**, 6449–6452.

101 K. Y. Zou, W. T. Deng, D. S. Silvester, G. Q. Zou, H. S. Hou, C. E. Banks, L. J. Li, J. G. Hu and X. B. Ji, Carbonyl chemistry for advanced electrochemical energy storage systems, *ACS Nano*, 2024, **18**, 19950–20000.

102 D. K. Hong, Y. Choi, J. Ryu, J. Mun, W. Choi, M. Park, Y. Lee, N. S. Choi, G. Lee, B. S. Kim and S. Park, Homogeneous Li deposition through the control of carbon dot-assisted Li-dendrite morphology for high-performance Li-metal batteries, *J. Mater. Chem. A*, 2019, **7**(35), 20325–20334.

103 J. Conder, R. Bouchet, S. Trabesinger, C. Marino, L. Gubler and C. Villevieille, Direct observation of lithium polysulfides in lithium-sulfur batteries using operando X-ray diffraction, *Nat. Energy*, 2017, **2**(6), 17069.

104 G. R. Li, S. Wang, Y. N. Zhang, M. Li, Z. W. Chen and J. Lu, Revisiting the role of polysulfides in lithium-sulfur batteries, *Adv. Mater.*, 2018, **30**(22), 1705590.

105 M. K. Rybarczyk, H. J. Peng, C. Tang, M. Lieder, Q. Zhang and M. M. Titirici, Porous carbon derived from rice husks as sustainable bioresources: insights into the role of micro-/mesoporous hierarchy in hosting active species for lithium-sulphur batteries, *Green Chem.*, 2016, **18**(19), 5169–5179.

106 H. Kim, J. Lee, H. Ahn, O. Kim and M. J. Park, Synthesis of three-dimensionally interconnected sulfur-rich polymers for cathode materials of high-rate lithium-sulfur batteries, *Nat. Commun.*, 2015, **6**, 7278.

107 J. J. Xu, Z. Li, P. Sun, K. Liu, Z. Q. Liu, Z. L. Hong and F. Q. Huang, Effective incorporation of nitrogen and

boron in worm-like carbon foam for confining polysulfides, *Carbon*, 2019, **155**, 379–385.

108 R. L. Bai, Q. S. Lin, X. Y. Li, F. X. Ling, H. J. Wang, S. Tan, L. X. Hu, M. Z. Ma, X. J. Wu, Y. Shao, X. H. Rui, E. Y. Hu, Y. Yao and Y. Yu, Toward complete transformation of sodium polysulfides by regulating the second-shell coordinating environment of atomically dispersed Fe, *Angew. Chem. Int. Ed.*, 2023, **62**(26), e202218165.

109 E. R. Zhang, X. Hu, L. Z. Meng, M. Qiu, J. X. Chen, Y. J. Liu, G. Y. Liu, Z. C. Zhuang, X. B. Zheng, L. R. Zheng, Y. Wang, W. Tang, Z. G. Lu, J. T. Zhang, Z. H. Wen, D. S. Wang and Y. D. Li, Single-atom yttrium engineering janus electrode for rechargeable Na-S batteries, *J. Am. Chem. Soc.*, 2022, **144**(41), 18995–19007.

110 Y. S. Zhang, X. L. Zhang, S. R. P. Silva, B. Ding, P. Zhang and G. S. Shao, Lithium-sulfur batteries meet electrospinning: Recent advances and the key parameters for high gravimetric and volume energy density, *Adv. Sci.*, 2022, **9**(4), 2103879.

111 Y. C. Ho and S. H. Chung, A design of the cathode substrate for high-loading polysulfide cathodes in lean-electrolyte lithium-sulfur cells, *Chem. Eng. J.*, 2021, **422**, 130363.

112 J. M. Chabu, K. Zeng, G. Y. Jin, M. Y. Zhang, Y. J. Li and Y. N. Liu, Simple approach for the preparation of nitrogen and sulfur codoped carbon dots/reduced graphene oxide as host for high-rate lithium-sulfur batteries, *Mater. Chem. Phys.*, 2019, **229**, 226–231.

113 F. Xie, Z. Xu, A. C. S. Jensen, F. X. Ding, H. Au, J. Y. Feng, H. Luo, M. Qiao, Z. Y. Guo, Y. X. Lu, A. J. Drew, Y. S. Hu and M. M. Titirici, Unveiling the role of hydrothermal carbon dots as anodes in sodium-ion batteries with ultrahigh initial coulombic efficiency, *J. Mater. Chem. A*, 2019, **7**(48), 27567–27575.

114 Y. P. Liu, F. Bettels, Z. H. Lin, Z. H. Li, Y. X. Shao, F. Ding, S. Y. Liu and L. Zhang, Recent advances in transition-metal-based catalytic material for room-temperature sodium-sulfur batteries, *Adv. Funct. Mater.*, 2024, **34**(5), 2302626.

115 Y. H. Zheng, Y. S. Wang, Y. X. Lu, Y. S. Hu and J. Li, A high-performance sodium-ion battery enhanced by macadamia shell derived hard carbon anode, *Nano Energy*, 2017, **39**, 489–498.

116 Z. Zheng, S. J. Hu, W. J. Yin, J. Peng, R. Wang, J. Jin, B. B. He, Y. S. Gong, H. W. Wang and H. J. Fan, CO_2-etching creates abundant closed pores in hard carbon for high-plateau-capacity sodium storage, *Adv. Energy Mater.*, 2024, **14**, 2303064.

117 H. N. He, D. Sun, Y. G. Tang, H. Y. Wang and M. H. Shao, Understanding and improving the initial Coulombic efficiency of high-capacity anode materials for practical sodium ion batteries, *Energy Storage Mater.*, 2019, **23**, 233–251.

118 S. C. Liang, S. Zhang, Z. Liu, J. Feng, Z. M. Jiang, M. J. Shi, L. Chen, T. Wei and Z. J. Fan, Approaching the theoretical sodium storage capacity and ultrahigh rate of layer-expanded MoS_2 by interfacial engineering on N-doped graphene, *Adv. Energy Mater.*, 2021, **11**(12), 2002600.

119 C. Chen, G. Q. Li, Y. Lu, J. D. Zhu, M. J. Jiang, Y. Hu, L. Y. Cao and X. W. Zhang, Chemical vapor deposited MoS_2/electrospun carbon nanofiber composite as anode material for high-performance sodium-ion batteries, *Electrochim. Acta*, 2016, **222**, 1751–1760.

120 C. T. Zhao, C. Yu, M. D. Zhang, Q. Sun, S. F. Li, M. N. Banis, X. T. Han, Q. Dong, J. Yang, G. Wang, X. L. Sun and J. S. Qiu, Enhanced sodium storage capability enabled by super wide-interlayer-spacing MoS_2 integrated on carbon fibers, *Nano Energy*, 2017, **41**, 66–74.

121 W. L. Xu, X. Zhao, F. Y. Zhan, Q. Q. He, H. Y. Wang, J. Chen, H. Y. Wang, X. H. Ren and L. Y. Chen, Toward emerging two-dimensional nickel-based materials for electrochemical energy storage: Progress and perspectives, *Energy Storage Mater.*, 2022, **53**, 79–135.

122 M. Q. Wang, B. Y. Qin, F. Xu, W. Yang, Z. T. Liu, Y. F. Zhang and H. S. Fan, Hetero-structural and hetero-interfacial engineering of MXene@Bi_2S_3/Mo_7S_8 hybrid for advanced sodium/potassium-ion batteries, *J. Colloid Interface Sci.*, 2023, **650**, 446–455.

123 Y. Q. Miao, X. S. Zhao, X. Wang, C. H. Ma, L. Cheng, G. Chen, H. J. Yue, L. Wang and D. Zhang, Flower-like $NiCo_2S_4$ nanosheets with high electrochemical performance for sodium-ion batteries, *Nano Res.*, 2020, **13**(11), 3041–3047.

124 F. Wang, X. L. Liu, G. G. Duan, H. Q. Yang, J. Y. Cheong, J. Lee, J. Ahn, Q. Zhang, S. J. He, J. Q. Han, Y. Zhao, I. D. Kim and S. H. Jiang, wood-derived, conductivity and hierarchical pore integrated thick electrode enabling high areal/volumetric energy density for hybrid capacitors, *Small*, 2021, **17**(35), 2102532.

125 J. Q. Yu, D. P. Cai, J. H. Si, H. B. Zhan and Q. T. Wang, MOF-derived $NiCo_2S_4$ and carbon hybrid hollow spheres compactly concatenated by electrospun carbon nanofibers as self-standing electrodes for aqueous alkaline Zn batteries, *J. Mater. Chem. A*, 2022, **10**(8), 4100–4109.

126 X. X. Zhou, Y. Wang, C. C. Gong, B. Liu and G. Wei, Production, structural design, functional control, and broad applications of carbon nanofiber-based nanomaterials: A comprehensive review, *Chem. Eng. J.*, 2020, **402**, 126189.

127 R. Huang, D. Yan, Q. Y. Zhang, G. W. Zhang, B. B. Chen, H. Y. Yang, C. Y. Yu and Y. Bai, Unlocking charge transfer limitation in NASICON structured $Na_3V_2(PO_4)_3$ cathode *via* trace carbon incorporation, *Adv. Energy Mater.*, 2024, **14**(21), 2400595.

128 Y. Su, B. Johannessen, S. L. Zhang, Z. R. Chen, Q. F. Gu, G. J. Li, H. Yan, J. Y. Li, H. Y. Hu, Y. F. Zhu, S. L. Xu, H. K. Liu, S. X. Dou and Y. Xiao, Soft- rigid heterostructures with functional cation vacancies for fast-charging and high-capacity sodium storage, *Adv. Mater.*, 2023, **35**(40), 2305149.

129 G. X. Chen, Q. Huang, T. Wu and L. Lu, Polyanion sodium vanadium phosphate for next generation of sodium-ion batteries-a review, *Adv. Funct. Mater.*, 2020, **30**(34), 2001289.

130 H. L. Xiong, G. Sun, Z. L. Liu, L. Zhang, L. Li, W. Zhang, F. Du and Z. A. Qiao, Polymer stabilized droplet

templating towards tunable hierarchical porosity in single crystalline $Na_3V_2(PO_4)_3$ for enhanced sodium-ion storage, *Angew. Chem. Int. Ed.*, 2021, **60**(18), 10334–10341.

131 H. J. Wang, J. Q. Gao, Y. Mei, L. S. Ni, Y. He, N. Y. Hong, J. N. Huang, W. T. Deng, G. Q. Zou, H. S. Hou, T. C. Liu, C. P. Liang, X. B. Ji and K. Amine, Halting oxygen evolution to achieve long cycle life in sodium layered cathodes, *Angew. Chem., Int. Ed.*, 2025, **64**, e202418605.

132 H. R. Ding, Y. J. Li, X. Y. Hu, J. Li, Z. L. Geng, Y. H. Liu, W. T. Deng, G. Q. Zou, L. Yang, H. S. Hou and X. B. Ji, In-situ constructing N,S-codoped carbon heterointerface for high-rate cathode of sodium-ion batteries, *ACS Appl. Mater. Interfaces*, 2024, **16**, 63655–63667.

133 H. Wang, Y. Mei, J. Gao, L. Ni, N. Hong, L. Ma, G. Kwon, J. Huang, Y. He and W. Deng, Entropy-tailored fast-charging sodium layered cathodes, *J. Am. Chem. Soc.*, 2025, **147**, 4810–4820.

134 S. Y. Liu, X. X. Cao, Y. P. Zhang, K. Wang, Q. Su, J. Chen, Q. He, S. Q. Liang, G. Z. Cao and A. Q. Pan, Carbon quantum dot modified $Na_3V_2(PO_4)_3F_3$ as a high-performance cathode material for sodium-ion batteries, *J. Mater. Chem. A*, 2020, **8**(36), 18872–18879.

135 J. C. Wang, X. D. Zhang, W. He, Y. Z. Yue, Y. Y. Wang and C. J. Zhang, Layered hybrid phase $Li_2NaV_2(PO_4)_3$/carbon dot nanocomposite cathodes for Li^+/Na^+ mixed-ion batteries, *RSC Adv.*, 2017, **7**(5), 2658–2666.

136 J. Zhang, Z. W. Zhao, Z. Yang, Y. Z. Chen, G. M. Zhong, L. M. Guo and Z. Q. Peng, A high-performance zinc anode enabled by carbon quantum dots with H_2O-structure-regulating capabilities, *Energy Storage Mater.*, 2023, **61**, 102904.

137 L. Ma, M. A. Schroeder, O. Borodin, T. P. Pollard, M. S. Ding, C. S. Wang and K. Xu, Realizing high zinc reversibility in rechargeable batteries, *Nat. Energy*, 2020, **5**(10), 743–749.

138 L. Yan, Y. Zhang, Z. G. Ni, Y. Zhang, J. Xu, T. Y. Kong, J. H. Huang, W. Li, J. Ma and Y. G. Wang, Chemically self-charging aqueous zinc-organic battery, *J. Am. Chem. Soc.*, 2021, **143**(37), 15369–15377.

139 X. Y. Wu, Y. K. Xu, C. Zhang, D. P. Leonard, A. Markir, J. Lu and X. L. Ji, Reverse dual-ion battery *via* a $ZnCl_2$ water-in-salt electrolyte, *J. Am. Chem. Soc.*, 2019, **141**(15), 6338–6344.

140 D. Kundu, B. D. Adams, V. Duffort, S. H. Vajargah and L. F. Nazar, A high-capacity and long-life aqueous rechargeable zinc battery using a metal oxide intercalation cathode, *Nat. Energy*, 2016, **1**, 16119.

141 G. Garcia, E. Ventosa and W. Schuhmann, Complete prevention of dendrite formation in Zn metal anodes by means of pulsed charging protocols, *ACS Appl. Mater. Interfaces*, 2017, **9**(22), 18691–18698.

142 A. R. Mainar, E. Iruin, L. C. Colmenares, A. Kvasha, I. de Meatza, M. Bengoechea, O. Leonet, I. Boyano, Z. C. Zhang and J. A. Blazquez, An overview of progress in electrolytes for secondary zinc-air batteries and other storage systems based on zinc, *J. Energy Storage*, 2018, **15**, 304–328.

143 P. Hu, M. Y. Yan, T. Zhu, X. P. Wang, X. J. Wei, J. T. Li, L. Zhou, Z. H. Li, L. N. Chen and L. Q. Mai, Zn/V_2O_5 aqueous hybrid-ion battery with high voltage platform and long cycle life, *ACS Appl. Mater. Interfaces*, 2017, **9**(49), 42717–42722.

144 X. X. Jia, C. F. Liu, Z. G. Neale, J. H. Yang and G. Z. Cao, Active materials for aqueous zinc ion batteries: synthesis, crystal structure, morphology, and electrochemistry, *Chem. Rev.*, 2020, **120**(15), 7795–7866.

145 C. Li, Z. T. Sun, T. Yang, L. H. Yu, N. Wei, Z. N. Tian, J. S. Cai, J. Z. Lv, Y. L. Shao, M. H. Rummeli, J. Y. Sun and Z. F. Liu, Directly grown vertical graphene carpets as janus separators toward stabilized Zn metal anodes, *Adv. Mater.*, 2020, **32**(33), 2003425.

146 Y. Qin, P. Liu, Q. Zhang, Q. Wang, D. Sun, Y. G. Tang, Y. Ren and H. Y. Wang, Advanced filter membrane separator for aqueous zinc-ion batteries, *Small*, 2020, **16**(39), 2003106.

147 L. B. Li, J. X. Peng, X. F. Jia, X. J. Zhu, B. C. Meng, K. Yang, D. W. Chu, N. X. Yang and J. Yu, PBC@cellulose-filter paper separator design with efficient ion transport properties toward stabilized zinc-ion battery, *Electrochim. Acta*, 2022, **430**, 141129.

148 L. J. Yang, J. H. Ma, Y. M. Liu, C. Y. Ma, X. Yu and Z. H. Chen, Low platinum loading electrocatalyst supported on a carrier derived from carbon dots doped ZIF-67 for the ORR and zinc-air batteries, *Nanoscale*, 2024, **16**(10), 5433–5440.

149 C. J. Yin, H. Wang, C. L. Pan, Z. Li and J. S. Hu, Constructing MOF-derived V_2O_5 as advanced cathodes for aqueous zinc ion batteries, *J. Energy Storage*, 2023, **73**, 109045.

150 D. Sun, M. Zhang, W. Wan, Y. L. Cao and H. Chai, Modified vanadium oxide with enhanced diffusion kinetic for high rate aqueous zinc-ion batteries, *J. Energy Storage*, 2023, **73**, 109236.

151 Y. Q. Yang, Y. Tang, G. Z. Fang, L. T. Shan, J. S. Guo, W. Y. Zhang, C. Wang, L. B. Wang, J. Zhou and S. Q. Liang, Li^+ intercalated $V_2O_5 \cdot nH_2O$ with enlarged layer spacing and fast ion diffusion as an aqueous zinc-ion battery cathode, *Energy Environ. Sci.*, 2018, **11**(11), 3157–3162.

152 J. Li, P. Guo, G. Chen, C. Wu, Y. Xiao, H. Dong, Y. Liang, Y. Liu, H. Hu and M. Zheng, Chitosan-derived carbon dots introduced V2O5 nanobelts for high-performance aqueous zinc-ion battery, *J. Energy Storage*, 2024, **84**, 110632.

153 J. R. Zhang, S. X. Wei, H. W. Wang, H. H. Liu, Y. Zhang, S. Y. Liu, Z. J. Wang and X. Q. Lu, Carbon quantum dots promote coupled valence engineering of V_2O_5 nanobelts for high-performance aqueous zinc-ion batteries, *Chemsuschem*, 2021, **14**(9), 2076–2083.

154 L. N. Chen, Y. S. Ruan, G. B. Zhang, Q. L. Wei, Y. L. Jiang, T. F. Xiong, P. He, W. Yang, M. Y. Yan, Q. Y. An and L. Q. Mai, Ultrastable and high-performance Zn/VO_2 battery based on a reversible single-phase reaction, *Chem. Mater.*, 2019, **31**(3), 699–706.

155 S. Liu, L. Kang, J. M. Kim, Y. T. Chun, J. Zhang and S. C. Jun, Recent advances in vanadium-based aqueous rechargeable zinc-ion batteries, *Adv. Energy Mater.*, 2020, **10**(25), 2000477.

156 T. H. Wu, J. A. Chen, J. H. Su and Y. H. Ting, Decorating carbon quantum dots onto VO_2 nanorods to boost electron and ion transport kinetics for high-performance zinc-ion batteries, *J. Energy Storage*, 2023, **74**, 109340.

157 C. M. Chen, Y. C. Yang, X. Tang, R. H. Qiu, S. Y. Wang, G. Z. Cao and M. Zhang, Graphene-encapsulated FeS_2 in carbon fibers as high reversible anodes for Na^+/K^+ batteries in a wide temperature range, *Small*, 2019, **15**(10), 1804740.

158 S. K. Chong, Y. F. Wu, S. W. Guo, Y. N. Liu and G. Z. Cao, Potassium nickel hexacyanoferrate as cathode for high voltage and ultralong life potassium-ion batteries, *Energy Storage Mater.*, 2019, **22**, 120–127.

159 Q. Y. Lin, Y. Wang, J. Du and A. B. Chen, Preparation of dispersed hollow carbon spheres assisted by silica/carbon shell isolation for supercapacitors, *Diam. Relat. Mater.*, 2023, **139**, 110346.

160 H. R. Wang, H. W. Zhou, M. Gao, Y. A. Zhu, H. T. Liu, L. Gao and M. X. Wu, Hollow carbon spheres with artificial surface openings as highly effective supercapacitor electrodes, *Electrochim. Acta*, 2019, **298**, 552–560.

161 Y. L. Wei, Q. Wang, Q. Liu, R. Z. Wang, Y. Wang, S. H. Luo, Y. H. Zhang, P. Q. Hou, S. X. Yan, X. Liu and J. Guo, Nano hollow carbon regulated by carbon dots as a high-performance anode for potassium and sodium ion battery, *Appl. Surf. Sci.*, 2024, **648**, 159017.

162 E. J. Zhang, X. N. Jia, B. Wang, J. Wang, X. Z. Yu and B. G. Lu, Carbon dots@rGO paper as freestanding and flexible potassium-ion batteries anode, *Adv. Sci.*, 2020, **7**(15), 2000470.

163 M. R. Wang, Y. Li, J. Fang, C. J. Villa, Y. B. Xu, S. Q. Hao, J. Li, Y. X. Liu, C. Wolverton, X. Q. Chen, V. P. Dravid and Y. Q. Lai, Superior oxygen reduction reaction on phosphorus-doped carbon dot/graphene aerogel for all-solid-state flexible Al-air batteries, *Adv. Energy Mater.*, 2020, **10**(3), 1902736.

164 Y. Chen, T. He, Q. M. Liu, Y. F. Hu, H. Gu, L. Deng, H. T. Liu, Y. C. Liu, Y. N. Liu, Y. Zhang, S. W. Chen and X. P. Ouyang, Highly durable iron single-atom catalysts for low-temperature zinc-air batteries by electronic regulation of adjacent iron nanoclusters, *Appl. Catal. B Environ.*, 2023, **323**, 122163.

165 C. X. Zhao, J. N. Liu, N. Yao, J. Wang, D. Ren, X. Chen, B. Q. Li and Q. Zhang, Can aqueous zinc-air batteries work at sub-zero temperatures?, *Angew. Chem. Int. Ed.*, 2021, **60**(28), 15281–15285.

166 Q. C. Wang, Y. P. Lei, Z. Y. Chen, N. Wu, Y. B. Wang, B. Wang and Y. D. Wang, Fe/Fe_3C@C nanoparticles encapsulated in N-doped graphene-CNTs framework as an efficient bifunctional oxygen electrocatalyst for robust rechargeable Zn-air batteries, *J. Mater. Chem. A*, 2018, **6**(2), 516–526.

167 M. H. Shao, Q. W. Chang, J. P. Dodelet and R. Chenitz, Recent advances in electrocatalysts for oxygen reduction reaction, *Chem. Rev.*, 2016, **116**(6), 3594–3657.